EarthArXiv Coversheet

Title: On the Origin of Holocene Sea-Level Transgressions in Formerly Glaciated Regions

Authors:
Samuel J. Chester
schester@ldeo.columbia.edu
Department of Earth and Environmental Science, Columbia University, New York, NY, USA

Jacqueline Austermann
Department of Earth and Environmental Science, Columbia University, New York, NY, USA

William J. D'Andrea
Lamont-Doherty Earth Observatory, Columbia University, New York, NY, USA

Andrew J. Lloyd
Lamont-Doherty Earth Observatory, Columbia University, NY, USA

Roger C. Creel
Department of Physical Oceanography, Woods Hole Oceanographic Institution, Falmouth MA, USA

This preprint is under review at Quaternary Science Reviews and is not peer reviewed

Highlights

On the Origin of Holocene Sea-Level Transgressions in Formerly Glaciated Regions

Samuel J. Chester, Jacqueline Austermann, William J. D'Andrea, Andrew J. Lloyd, Roger C. Creel

- GIA models simulate the migration of the peripheral bulge (subsiding regions around former ice sheets) first towards and then away from a melting ice sheet during deglaciation ('reverse migration').
- We show how reverse migration arises from the competing rates of deformation in layers of the mantle with different viscosities.
- Holocene transgressions in formerly glaciated regions (RSL rise culminating in a high stand) are shown to be the result of reverse migration.
- We constrain radial mantle viscosity structure by comparing model predictions of the transgression to geologic constraints on transgression magnitude.

On the Origin of Holocene Sea-Level Transgressions in Formerly Glaciated Regions

Samuel J. Chester[a,*], Jacqueline Austermann[a], William J. D'Andrea[a], Andrew J. Lloyd[a], Roger C. Creel[a,b]

[a] *Lamont-Doherty Earth Observatory, Columbia University, 61 Rte 9W, Palisades, 10964, NY, USA*
[b] *Woods Hole Oceanographic Institution, Woods Hole, 02543, MA, USA*

Abstract

Over glacial cycles, the growing and shrinking of ice sheets has caused relative sea level (RSL) to differ from global mean sea level (GMSL) due to glacial isostatic adjustment (GIA), which depends on the viscoelastic properties of the solid Earth. During the last termination and through the Holocene, GIA-related isostatic uplift caused RSL to fall in regions formerly covered by ice sheets. Surrounding these uplifting regions is a narrow band of land where postglacial RSL fall was interrupted during the Holocene by a period of sea-level rise (i.e., a transgression) that culminated in a high stand before sea-level fall resumed. Holocene transgressions and high stands have been well documented in many locations including Norway, the Canadian Atlantic coast, the Canadian Pacific coast, Svalbard, the Baltic Sea, and the British Isles. A leading hypothesis poses that transgression occurred when GMSL rise outpaced isostatic rebound. We investigate the origins of these Holocene transgressions using GIA modeling and test the alternative hypothesis that they are predominantly the result of solid earth deformation. Our results highlight a unique pattern of solid earth deformation in which the region of subsidence (peripheral bulge) surrounding the ice sheet migrates first towards and then away from the melted ice mass. We show how this effect, which we term 'reverse migration', is the direct result of the contrast in viscosity between the upper and lower mantle. We compare our GIA model predictions of RSL change to two datasets: 1) RSL data from the last glacial maximum to present and 2) specific constraints on the transgression magnitude in Norway and Eastern Canada. Both datasets better fit RSL predicted by GIA models that include a mantle with a substantial (order of magnitude) increase in viscosity with depth over GIA predictions that don't include a contrast in mantle viscosity. We argue that this is a useful constraint on the local viscosity structure. Further, this suggests that in contrast to the conventional view that Holocene transgressions record GMSL temporarily outpacing isostatic uplift, solid earth deformation and specifically reverse migration played an important role in generating near-field Holocene transgressions.

Keywords: Holocene, Sea-Level change, Glacial isostatic adjustment, North America, Scandinavia, modeling, Transgression, High stand

1. Introduction

Since the Last Glacial Maximum (LGM), melting ice sheets have raised global mean sea level (GMSL) due to the addition of water mass to the oceans. The spatial patterns of changing relative sea level (RSL; sea level at a given location measured relative to present day), however, vary drastically as a result of glacial isostatic adjustment (GIA): the response of the solid Earth, the gravity field, and Earth's rotational axis to changes in ice and ocean loads (Farrell and Clark, 1976). Patterns of RSL change are fundamental to our understanding of the cryosphere, the viscoelastic structure of the solid Earth, and past human migration (Gomez et al., 2010; Lau et al., 2016; Borreggine et al., 2022).

*Corresponding author
Email address: schester@ldeo.columbia.edu (Samuel J. Chester)

GIA-related sea-level signatures depend on a site's proximity to former ice sheets. During glacial periods, ice sheets depress the solid Earth and displace mantle material laterally to form a surrounding uplifted region called the 'peripheral bulge'(Jamieson, 1882). Following ice sheet retreat, areas formerly under ice uplift rapidly and experience falling RSL at a decaying rate. By contrast, areas adjacent to former ice sheets undergo RSL rise during deglaciation at rates greater than GMSL rise due to the collapsing peripheral bulge. The rates of uplift and subsidence in these areas are controlled by the Earth's elastic and viscous properties. At locations far from former ice sheets, RSL rise closely resembles GMSL rise. However, there too GIA causes modifications. For example, a mid-Holocene high stand observed along low latitude coastlines is explained by 'ocean siphoning' and 'continental levering', processes related to the redistribution of water mass due to peripheral bulge subsidence and ocean loading, respectively (Mitrovica and Milne, 2002). The GIA process allows us to use these near-field and far-field RSL observations to constrain two important aspects of the Earth system: the history of ice sheets and the rheological properties of Earth's interior.

The margins immediately surrounding former ice sheets have particularly complex sea-level dynamics because, following ice margin retreat, the region of subsidence associated with the collapsing peripheral bulge gradually moves towards the region of ice loss—a process known as 'peripheral bulge migration' (Clark et al., 1978). This results in a characteristic RSL signal near former ice sheet margins: RSL initially falls during the deglaciation due to isostatic uplift (and the lost gravitational attraction of the ice sheet) and then rises once the subsidence is established in the region. The areas that experience peripheral bulge migration are generally understood to surround regions that exclusively experience isostatic uplift (RSL fall; Clark et al., 1978).

Yet another characteristic RSL signal is recorded in the zone between the area of isostatic uplift and the region of peripheral bulge migration. There, postglacial RSL fall is interrupted by early-mid Holocene (i.e. ∼10 - 4 ka) RSL rise followed by RSL fall to present (Fig. 1). These regions are found just inside the LGM extent of the ice sheets that covered Fennoscandia, Svalbard, the British Isles, and Canada (Forman, 2004; Smith et al., 2011; Shugar et al., 2014; Shennan et al., 2018; Vacchi et al., 2018; Rosentau et al., 2021; Creel et al., 2022). Observations used to constrain the timing and magnitude of these periods of RSL rise include lake and wetland sediment stratigraphy, elevation and deformation of high stand shorelines, and archeological data (e.g. Møller, 1987; Dionne, 1988; Rasmussen et al., 2018; Khan et al., 2019). Following the nomenclature long used in the scientific literature (e.g. Svendsen and Mangerud, 1987; Yu et al., 2007; Rosentau et al., 2021; Creel et al., 2022), we refer to the period of rising RSL culminating in a Holocene high stand as a 'transgression' (e.g., The 'Tapes Transgression' in Norway).

Though varying in timing and magnitude, the near-field Holocene transgressions share similarities. First, they occur thousands of years after local ice sheet retreat, indicating that they are not caused by ice readvance. Second, their magnitude increases with distance from the ice mass center (Rosentau et al., 2021; Creel et al., 2022). Third, they lie ice-ward of regions that record the typical peripheral bulge migration described above.

While GIA modeling has reproduced near-field Holocene transgressions in some locations, their causes remain debated (Kuchar et al., 2012; Shennan et al., 2018; Fjeldskaar and Bondevik, 2020). A leading hypothesis holds that near-field transgressions occurred when GMSL rise temporarily outpaced local isostatic uplift (James et al., 2007; Lambeck et al., 2010; Smith et al., 2011; Murray-Wallace and Woodroffe, 2014; Shennan et al., 2018; Fjeldskaar and Bondevik, 2020). In this view, the magnitude and timing of the transgression might be modulated by GIA processes, but its occurrence requires substantial concurrent GMSL rise and is not produced by GIA alone (Fig. 2A,B). This perspective is supported by the coincidence of slowing rates of GMSL rise between 7 and 5 ka and transgression maxima in many regions (Smith et al., 2011; Lambeck et al., 2014; Creel et al., 2023). The timing of the observed Holocene transgressions is, however, not globally synchronous. In Eastern Canada, for example, a high stand is dated to ∼4 ka, thousands of years after GMSL neared present levels (Dionne, 1988; Vacchi et al., 2018).

An alternative hypothesis is that solid earth deformation, specifically a migrating peripheral bulge, generated the Holocene transgression and subsequent high stand (Creel et al., 2022). In Norway, previous authors have dismissed the idea that the peripheral bulge may be responsible for the well-documented Tapes transgression based on modeling that suggests the peripheral bulge was either minimal or did not migrate onto land during the deglaciation (Fjeldskaar, 1994; Fjeldskaar and Bondevik, 2020). Along the

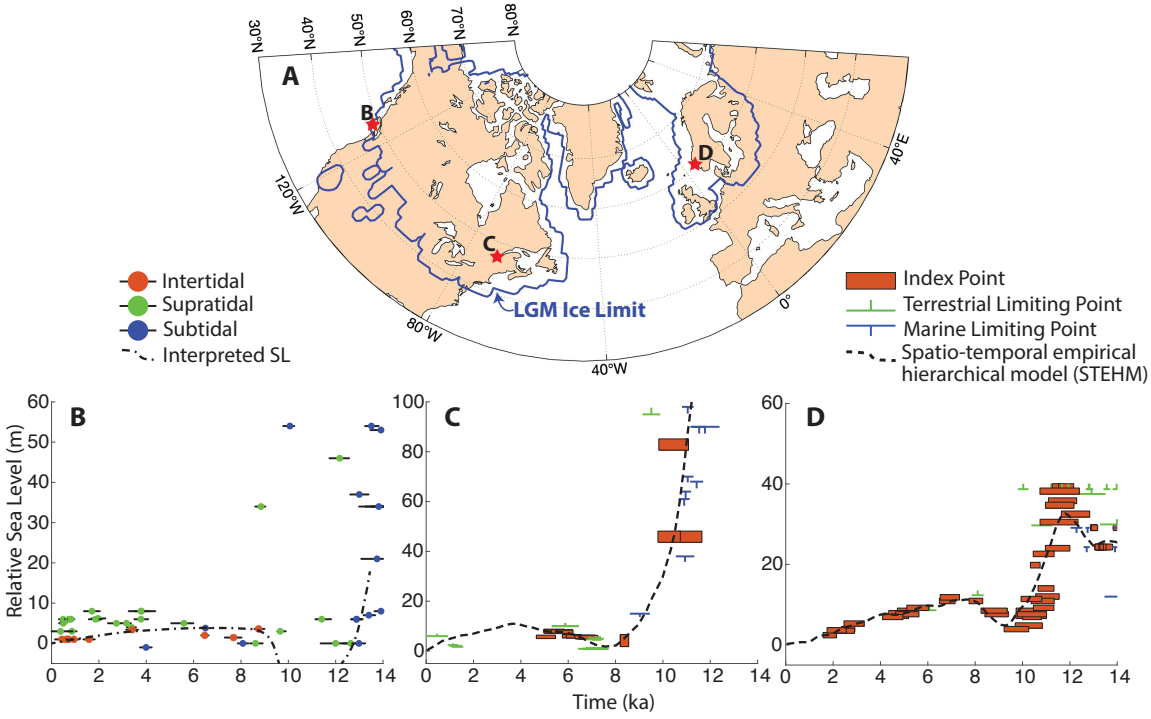

Figure 1: **Sea-level observations from the margins of formerly glaciated regions show a characteristic pattern of RSL fall punctuated by a period of RSL rise (transgression) during the Holocene.** Blue line in the top panel indicates the LGM ice limit from the ICE7G reconstruction (Roy and Peltier, 2018). Sea-level data and curves for three sites, and terminology used to classify these data, are from (B) Shugar et al. (2014) and references therein, (C) Vacchi et al. (2018) and references therein, and (D) Creel et al. (2022) and references therein. All three plots show data from within a small region and elevations are not corrected for spatial variations in GIA.

US east coast, RSL observations and GIA modeling suggests that the peripheral bulge migrated hundreds of kilometers towards the former ice mass, but this has not been specifically investigated in the context of the Holocene transgression recorded in the gulf of St. Lawrence (Barnhardt et al., 1995; Quinlan and Beaumont, 1981, 1982; Dionne, 1988; Baril et al., 2023). The signal of peripheral bulge subsidence is well documented in other locations as well, including the Baltic Sea, the British Isles and west coast of North America, but has only ever been attributed to the typical pattern of RSL fall followed by RSL rise until present (Engelhart and Horton, 2012; Engelhart et al., 2015; Shennan et al., 2018; Rosentau et al., 2021). This is likely because, as previous authors noted, it is not intuitively obvious why peripheral bulge migration would lead to a Holocene transgression culminating in a high stand.

One way solid earth deformation could generate a Holocene transgression is by causing the 'hinge line'—the line delineating uplifting regions that were below former ice sheets and subsiding regions associated with the peripheral bulge—to migrate first toward and then away from the center of the former ice sheet (Fig. 2C,D). Any region through which the hinge line crosses first by 'ice-ward migration' (toward the former ice sheet) and then again in the reverse direction would sequentially undergo uplift, subsidence, and uplift, i.e. a Holocene transgression. We term this process 'reverse migration'. Of course, the details of how hinge line migration affects RSL recorded at a given location is complicated by GMSL changes and other GIA related processes including water loading and gravity changes.

In this study, we test the hypothesis that Holocene transgressions are caused by reverse migration. Using a set of modeling experiments with increasing complexity, we investigate how reverse migration arises as a solid earth response to deglaciation, and then link that process to predicted RSL. Comparing the predicted transgressions from GIA models with the geologic record, we find that only models with reverse migration of

the peripheral bulge successfully reproduce the observations. Finally, we illustrate how this understanding can be used to constrain the stratification of viscosity in Earth's mantle.

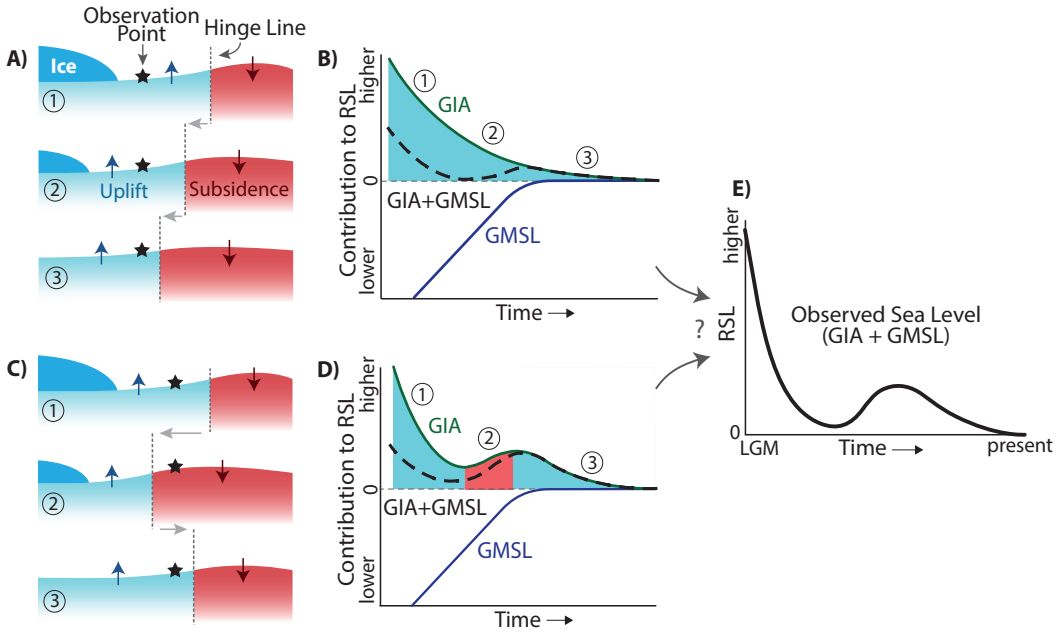

Figure 2: **Competing hypotheses for the origin of Holocene transgressions. (A/B)** Illustration of the hypothesis that an RSL oscillation is caused by GMSL rise temporarily outpacing isostatic uplift. (A) The observation point (black star) remains in the uplifting region during (1), (2), and (3), successive deglaciation time steps. (B) RSL at the observation point, separated into the influence of GIA and GMSL. The rate of GMSL rise exceeds isostatic uplift at time 2, resulting in a combined RSL signal that includes an RSL oscillation as illustrated in (E). **(C/D)** Conceptual model showing how reverse migration of the hinge line (the line dividing uplift and subsidence) can generate an oscillation. (C) During deglaciation, the hinge line migrates over the observation point twice, resulting in discrete periods of uplift and subsidence. The influence of GIA and GMSL at this observation point is conceptualized in (D). The combined GIA and GMSL signal result in an RSL oscillation (E).

2. Methods

To investigate the mechanisms driving Holocene sea-level changes within formerly glaciated regions, we use three different GIA models, which vary in their complexity and ability to map flow within the Earth. This allows us to tease out fundamental processes before incrementally building up to a more physically complete treatment of GIA. In this section, we will first describe the three models and the experiments conducted with each. We then pair the most physically complete of the three models with sea-level observations to validate the findings from the modeling experiments and investigate constraints on local mantle viscosity.

2.1. GIA Model Description

We conduct modeling experiments using three GIA models that allow us to target specific processes and regions of the Earth. In all instances, we perform simulations that adopt a spherically symmetric earth structure to determine the response of the solid Earth and its gravitational field to surface load changes. Two of the codes are run without an ocean (or a distant one) and thus, solve for surface deformation and gravity perturbations arising only from changes in the ice load. One of these codes is used to determine the deformation throughout the mantle, while the other, being computationally faster, is used to determine only surface deformation for a wider range of Earth models. These models do not account for changes in Earth's rotation due to surface load changes. The third model includes an evolving ocean and accounts for rotation

changes. This last model follows the sea-level theory proposed by Farrell and Clark (1976) and extended by Mitrovica and Milne (2003), Kendall et al. (2005), Dalca et al. (2013). We describe these models in greater detail below.

The first model—hereafter the 'numerical model, no oceans' (NM-NO)—calculates surface deformation and gravity field changes using a numerical approach that does not employ normal modes. The model solves the rate formulation of the GIA problem in which scalar, vector, and tensor fields are represented using the canonical basis vectors of Phinney and Burridge (1973), which rely on generalized spherical harmonics (Al-Attar and Tromp, 2014; Crawford et al., 2018; Lloyd et al., 2023). The code was designed for inverse modeling using adjoint methods. However, in this study, we only solve the forward GIA problem (for details, see Crawford et al., 2018). This model is chosen because it directly outputs the full mantle flow field, which allows mapping and investigating deformation below melting ice sheets. The code's implementation includes an ocean, but we place the ocean and ice sheet in opposite hemispheres, that have topography of -10 m and 1,000 km plateau, respectively. As such, solid earth deformation beneath and around the ice sheet is due only to ice mass change and not ocean loading.

The second model, hereafter the 'love-number no-oceans' (LN-NO) model, follows the normal mode approach, which uses Green's functions (Peltier, 1974; Peltier and Andrews, 1976). We convolve the ice load changes with the corresponding love numbers to obtain surface deformation and gravity field changes. This model does not include oceans and is conceptually analogous to the NM-NO model in the near-field processes and physics accounted for, but its semi-analytical approach makes it more efficient, which allows us to explore a large suite of earth structures. We tested the LN-NO and NM-NO models for a range of Earth parameters to demonstrate consistency between the two (Fig. S1).

The third model, hereafter the 'love-number sea-level' (LN-SL) model, uses the same approach as the second model but introduces oceans and solves the sea-level equation, originally described by Farrell and Clark (1976). This allows us to investigate the relative importance of ice loading, ocean loading, and GMSL changes. The model, which employs an algorithm described in Kendall et al. (2005) and Dalca et al. (2013), solves for a dynamically evolving ocean that follows the gravitational equipotential surface. The code enforces mass conservation between oceans and ice sheets, includes shoreline migration and rotational effects, and checks for floating ice (Dalca et al., 2013). Modern-day topography is represented by the global relief model, ETOPO1 (Amante and Eakins, 2009).

2.2. Model Inputs

In all three models, Earth rheology is described using a constitutive relationship for an isotropic, linear viscoelastic material and is assumed to be radially symmetric (1-D; Peltier, 1974). The elastic and density structure are taken from the Preliminary Reference Earth Model (PREM; Dziewonski and Anderson, 1981). The viscosity structure and lithospheric thickness parameters are varied in each experiment (Table 1). Lateral variations in mantle viscosity are known to affect sea-level predictions in GIA models (e.g., Latychev et al., 2005; Austermann et al., 2013). However, a 1-D structure can still capture much of the GIA signal in regional sea-level records (e.g., Davis and Mitrovica, 1996; Kendall et al., 2005; Shennan et al., 2018), and the computational efficiency of 1-D models allows us to test a broader range of rheological parameters. We emphasize that our aim is to investigate mid-Holocene transgressions on a process level; employing a 3-D earth structure could improve the accuracy of a global simulation aimed at each transgression simultaneously, but is not expected to change the processes that generate the observed sea-level trend.

The GIA simulations are forced with prescribed ice histories. This includes a synthetic loading history, hereafter the 'disc load', and a realistic global ice sheet reconstruction, ICE7G (Roy and Peltier, 2017). The disc load is a parabolic disc centered on the South Pole with a maximum thickness of 3000 m. The timing, magnitude, and geometry is chosen to represent a simplified version of Northern Hemisphere ice sheets through the last glacial cycle. To maintain consistency with subsequent experiments, we express time as thousands of years before 1950 (ka). Ice thickens linearly from 230 m at 60 ka to maximum thickness at 21 ka, followed by linear retreat and thinning until disappearing at 8 ka (see Appendix A for details). ICE-7G spans 26 ka to present and is derived from geologic constraints on ice-sheet geometry and ice thickness (Roy and Peltier, 2018). We extend the model from 26 to 122 ka using the sea-level reconstruction from Waelbroeck et al. (2002) and by assuming that pre-LGM ice sheet geometry is similar to post-LGM for the

Table 1: Table 1. Summary of GIA modeling experiments. For each experiment, the processes included in the model are summarized as well as the model inputs (ice model and earth structure parameters). LT = Lithospheric Thickness, UMV = Upper Mantle Viscosity, LMV = Lower Mantle Viscosity

.

Experiment Name	Overview of Model Processes	Ice Model Input	Earth Structure Input		
			LT (km)	UMV (10^{21} Pa s)	LMV (10^{21} Pa s)
NM-NO - Disc Load	- Solid earth deformation due to ice load	Disc load	100, 140	0.4, 1	1, 4, 20
LN-NO - Disc Load	- Gravitational changes due to ice and Earth mass	Disc load	60, 80, 100, 120, 140, 160	0.1, 0.2, 0.4, 0.7, 1, 2, 4	1, 2, 4, 7, 10, 20, 40, 70, 100
LN-NO - ICE7G	- No ocean (no hydrostatic loading, eustatic sea-level changes)	ICE7G			
LN-SL - ICE7G	- Solid earth deformation and gravity changes due to ice and ocean loads - Solves the full 'sea-level equation' - Dynamic ocean, water/ice mass conserved - Rotational feedbacks included	ICE7G ANU-7G PAT-7G			

same GMSL. We use 'ICE7G' hereafter to refer to this extended model. For sensitivity testing, we use two additional ice sheet reconstructions, one for the Laurentide ice sheet (LIS) (Lambeck et al., 2017), and one for the Eurasian ice sheet (EIS) (Patton et al., 2017). We combine these reconstructions with the remaining ice sheets from (the extended) ICE7G to create two new global reconstructions, hereafter ANU-7G and Patton-7G.

The LN-NO and LN-SL models are run at spherical harmonic degree 256, which corresponds to a spatial resolution of ∼80 km (half a wavelength). For computational efficiency, the NM-NO model is run at spherical harmonic degree 128 (spatial resolution of ∼155 km, half a wavelength). The ice loads and modern-day topography are linearly interpolated to match these resolutions.

2.3. GIA Model Experiments

We run four experiments with an increasingly accurate physical treatment of GIA and ice histories to understand how solid earth deformation at depth relates to realistic predictions for RSL changes during the deglaciation. The experiments are described below and summarized in Table 1.

1. *NM-NO - Disc Load:* We first seek to understand how deformation through the mantle and lithosphere causes surface displacement. We perform NM-NO model simulations with the disc load and varying rheological parameters: lithospheric thickness (LT), upper mantle viscosity (UMV), and lower mantle viscosity (LMV).
2. *LN-NO - Disc Load:* The second experiment is designed to further explore the sensitivity of surface deformation to rheological parameters. Using the LN-NO model, we run disc load simulations with a more extensive range of parameters.
3. *LN-NO - ICE7G:* The third experiment introduces a data-constrained, realistic ice sheet reconstruction. The LN-NO model is run with the same viscosity and lithospheric thickness parameters as the last experiment but with the ICE7G model. We perform runs with only the Eurasian Ice Sheet (EIS) and runs including all ice sheets.
4. *LN-SL - ICE7G:* Finally, we add the GIA feedbacks encompassed in the gravitationally self-consistent LN-SL model. The LN-SL model is run with the same suite of rheological parameters as the LN-NO simulations and the full ICE7G reconstruction.

2.4. Model - Data Comparison

After understanding the fundamental processes that drive Holocene sea-level transgressions and high stands, we use the LN-SL model to compare model predictions to observations. We perform two goodness-of-fit tests between predicted RSL change and RSL data from the geologic record. The first test identifies the range of model inputs that best match post-glacial sea level observations and investigates the model sensitivity to input parameters. The second test examines the findings of the previous experiments by identifying the viscosity structure necessary to specifically match the location and magnitude of each observed transgression. We focus on two locations where the mid-Holocene transgression is prominent and well-documented: Norway and Eastern Canada.

2.4.1. Model fit to RSL data

To identify the range of model parameters that fit the available data in Norway and Eastern Canada, we compare LN-SL model results to two RSL datasets spanning the entire deglacial period (Vacchi et al., 2018; Creel et al., 2022). We explore the range of Earth rheology parameters in Table 1 and three ice sheet reconstructions (ICE7G, PAT-7G, and ANU-7G) described in section 2.2. Misfit between predictions and sea-level index points (SLIPs) is calculated using a weighted residual sum of squares (WRSS) approach following Auriac et al. (2016) and Creel et al. (2022):

$$WRSS_{nm} = \left(\frac{2r^t_{nm}}{e^t_n}\right)^2 + \left(\frac{2r^y_{nm}}{e^y_n}\right)^2 \tag{1}$$

where e^t_n and e^y_n are the data errors in time and elevation, respectively, and r^t_{nm} and $r^y_{nm}$are residuals in time and elevation, respectively, for a given model prediction m and SLIP n. Residuals are found by minimizing the distance between the SLIP and the predicted sea-level curve in elevation-age space. To extract the predicted sea-level curve, the model predictions are linearly interpolated in space and time to the specific location where the data was collected. A chi-squared metric is then calculated for each GIA model as follows

$$\chi^2_m = \frac{1}{N}\sum_{n=1}^{N} WRSS_{nm} \tag{2}$$

where N is the total number of SLIPs in the dataset. Lower chi-squared values indicate a better model fit to the RSL data.

2.4.2. Model fit to transgression magnitude

We perform a second test to identify the GIA models that best reproduce the observed Holocene transgressions and assess whether those models differ from the best-fitting models of the first test. We compare model predictions of the transgression magnitude (difference in elevation between sea-level low stand to following high stand) against observed magnitude. Determining observed magnitude at a particular site is challenging because continuous sea-level curves often must be constructed from multiple data points spanning a large area and several thousand years. Additionally, the greatest low stand or high stand is not necessarily recorded in a given region. To overcome this challenge, we use published Spatio-Temporal Empirical Hierarchical statistical Models (hereafter 'STEHMs') that interpolate sea-level data across space and time using a Bayesian approach. Both Creel et al. (2022) and Vacchi et al. (2018) report these models for Norway and Eastern Canada, respectively. While their methodology for constructing the posterior estimate of mean RSL and uncertainty is slightly different, they both provide data-informed estimates of RSL change that incorporate prior information from GIA models.

In Norway, the STEHM is available over the entire coastal region from 16 ka to the present in gridded data format. We identify the transgression magnitude in the STEHM by searching each grid point for a local minimum between 13 and 6 ka and a local maximum between 9 and 2 ka. Regions without a transgression are assigned zero magnitude. Predictions using the LN-SL model predictions are linearly interpolated to the grid resolution of the STEHM and the magnitude of transgressions are extracted using the same technique. We calculate misfit for each model run by taking the sum of squares of residuals between the transgression magnitude predicted by the STEHM and that predicted by the GIA model for each grid point in the domain.

For Eastern Canada, the entire STEHM is unavailable but is reported for seven locations. In three of these locations, local sea-level data and statistical modeling support a mid-Holocene transgression. Three other locations also suggest a transgression based on the STEHM but have no or few SLIPs that constrain the transgression. A seventh location has no evidence for a Holocene transgression culminating in a high stand and is included here as a spatial constraint. Comparison to model results follows the method applied for Norway.

3. Results

3.1. GIA Model Results

We explore the origin of Holocene sea-level transgressions in formerly glaciated regions by building up from simplified descriptions of GIA to ones that incorporate more fully capture the physical process of GIA. To investigate the hypothesis that solid earth deformation causes the Holocene transgressions, we focus on the evolution of the hinge line, which - as defined above - is the region that delineates solid Earth uplift from subsidence. When and how many times the hinge line crosses a region dictates the pattern of vertical deformation and may influence whether a transgression occurs (Fig. 2).

3.1.1. NM-NO - Disc Load

NM-NO simulations forced by a simplified ice sheet history help us understand how viscoelastic solid earth deformation produces patterns of vertical displacement on Earth's surface. During the initial deglaciation, a large region of uplift develops below the retreating ice sheet, which extends from the surface through the lower mantle (Fig. 3). Mantle material flows towards this region of mass loss generating a peripheral region of subsidence at the surface. As deglaciation progresses, different deformation patterns emerge depending on the viscosity structure. For models with a homogeneous mantle (isoviscous), the region of uplift shrinks and the surrounding region of subsidence expands to greater depths and moves iceward through the mantle and lithosphere. On Earth's surface, this contracting region of uplift manifests as iceward migration of the hinge line (black arrows, Fig. 3A).

In models with a viscosity increase across the transition zone at 670 km, the region of uplift shrinks faster in the upper mantle relative to the lower mantle (Fig. 3B). This difference in response times creates an intermediate zone where the surface, lithosphere, and upper mantle are all subsiding (red colors in Fig. 3B) while the lower mantle material is still moving upwards (turquoise colors in Fig. 3B). Near the termination of ice melt, the uplifting region in the upper mantle begins to expand again while the region of uplift in the lower mantle continues to contract. On the surface, this manifests as the hinge line migrating away from the ice sheet, i.e. reverse migration (Fig. 3B, inset 1 and 2).

3.1.2. LN-NO - Disc Load

We identify the parameters that generate reverse migration of the hinge line with the disc load by extending this analysis to a range of solid earth structures. Figure 4A shows hinge line location through time for simulations with a lithospheric thickness of 100 km and the full range of mantle viscosities (Table 1). Two sets of hinge line pathways emerge: hinge lines either migrate ice-ward continuously (Fig. 4A, light blue lines) or migrate first towards then away from the ice sheet (Fig. 4A, orange lines). The timing of migration reversal depends on solid earth parameters, but all reversals occur within a few thousand years of the time of final ice melt.

The distance that the hinge line travels away from the ice sheet following reversal and whether migration reverses at all is shown in Figure 4B. Models with insufficient contrast (approximately less than an order of magnitude) in upper vs. lower mantle viscosity do not produce reverse migration. Of the models that do, the amount of reverse migration depends primarily on the upper mantle viscosity but is also sensitive to lower mantle viscosity and lithospheric thickness.

Using the LN-NO model, we also calculate gravity perturbations associated with ice mass loss and earth mass redistribution, but find that including gravity does not change the observation that reverse migration depends primarily on mantle viscosity contrast (Fig. S2).

3.1.3. LN-NO - ICE7G

Simulations with a realistic ice history give similar, albeit more variable, results to the disc load model. Similar to the disc load experiments, each hinge line either migrates ice-ward continuously or initiates reverse migration around the time that the FIS disappears from Scandinavia (Fig. 5A). Though the results are more spatio-temporally variable due to the introduction of a realistic ice history, reverse migration still depends on the contrast between upper and lower mantle viscosity (Fig. 5B), and including gravitational effects does not reduce this dependency (Fig. S3). We also test the inclusion of all of Earth's ice sheets (i.e., the full

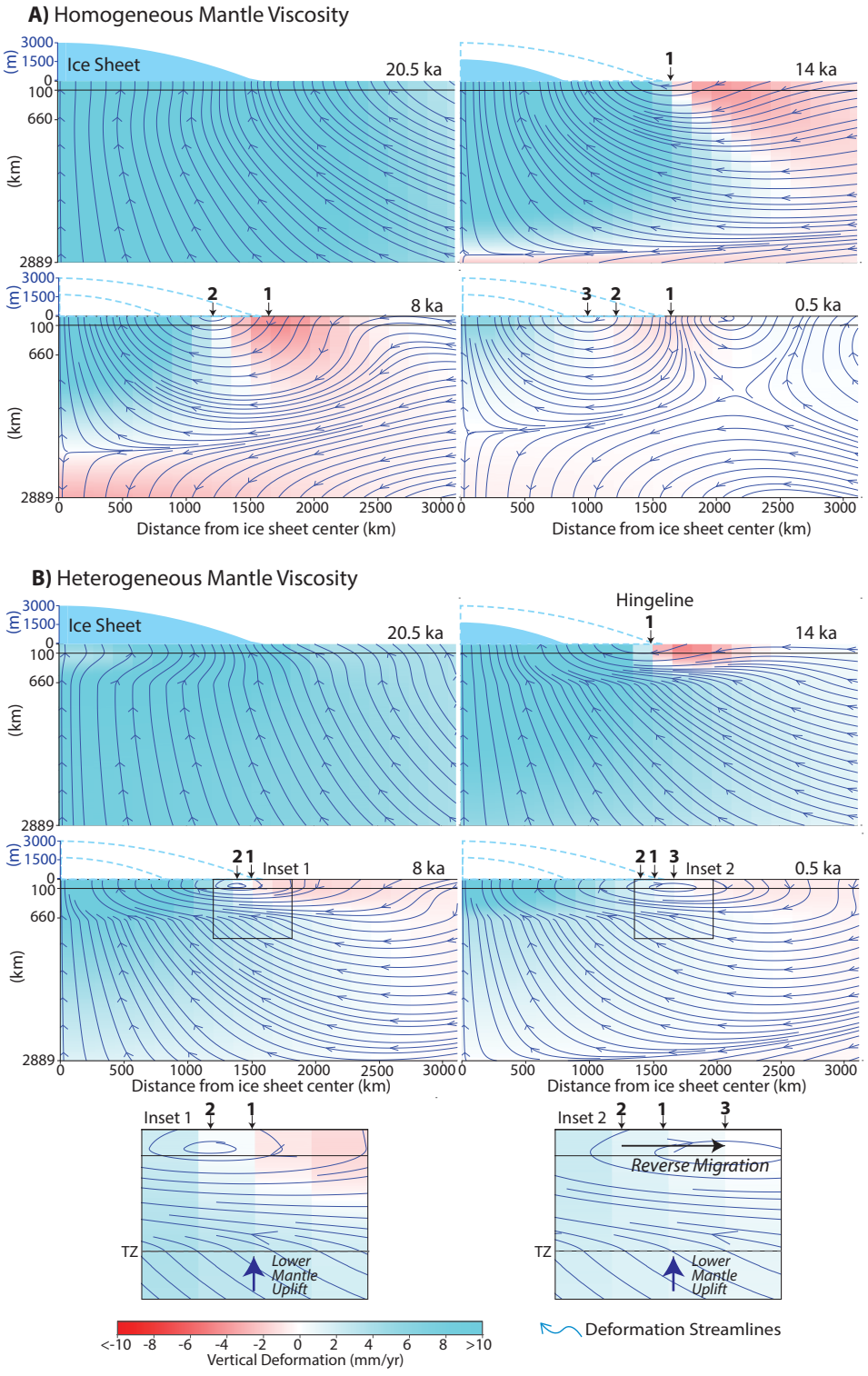

Figure 3: (Caption next page.)

Figure 3: **Solid earth deformation during ice melt depicted in a cross-section and calculated using the NM-NO code with a synthetic disc load.** The model contains effectively no ocean (see section 2.1). (A) Deformation for a model with a lithospheric thickness of 100 km, and a single mantle viscosity of $1 * 10^{21}$ Pa s. (B) Deformation for a model with a lithospheric thickness of 100 km, upper mantle viscosity of $0.4*10^{21}$ Pa s, and lower mantle viscosity of $10*10^{21}$ Pa s. Snapshots are shown at 20.5 ka, 14 ka, 8 ka, and 0.5 ka, where ka denotes thousands of years before the end of the simulation, which is meant to approximate the last glacial cycle. The rate of vertical deformation at each time step (color bar) and deformation field (blue streamlines) were calculated by differencing the total deformation at the given time with the previous time step (500 years earlier). Ice sheet extent (light blue) and thickness is indicated by the blue axis. Dashed blue lines show ice thicknesses in earlier snapshots. Downward arrows indicate the position of the hinge line and are numbered consecutively.

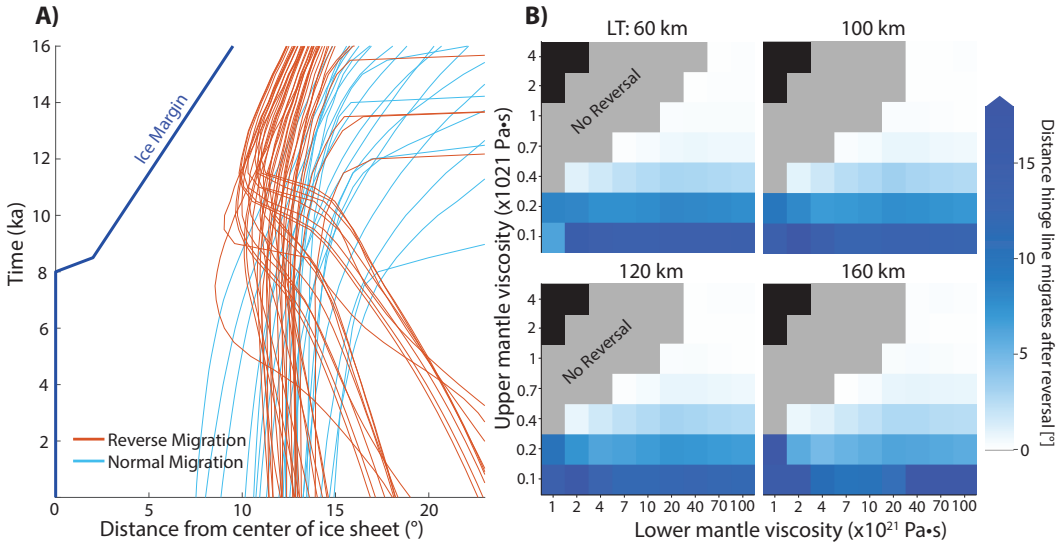

Figure 4: **LN-NO model predictions for the evolution of the solid earth hinge line during the deglaciation of a synthetic disc load.** The model includes no ocean. (A) Distance through time of the hinge line from the center of maximum ice thickness. Orange lines mark simulations that predict reverse migration. Simulations without reverse migration are in light blue. Dark blue line denotes the ice margin position. For clarity, only models with 100 km lithospheric thickness are shown. (B) Reverse migration distance as a function of upper and lower mantle viscosity and lithospheric thickness (LT). Grey indicates simulations where no reverse migration occurs. Black indicates simulations that were not run due to an inverted viscosity structure. Only the solid earth deformation is considered here; see Figure S2 for a version that includes gravitational effects.

ICE7G model) and find that it does not change the results for most earth structures (Fig. S4). Only with unrealistically high upper mantle viscosities ($>$ 4*10^{2}1 Pa s) do the Greenland and Laurentide ice sheets perturb hinge line evolution and drive reverse migration.

3.1.4. LN-SL - ICE7G

The LN-SL model, which includes a gravitationally self-consistent ocean, accounts for GMSL change, hydrostatic loading, migrating coastlines, and changes in Earth's rotational axis. Because this model predicts RSL change rather than solid earth deformation, we now consider the evolution of the 'sea-level hinge line' (the line delineating RSL rise and fall), which is influenced by solid earth deformation, changes in GMSL and other GIA processes (Table 1). Note that reverse migration of the sea-level hinge line results in a Holocene transgression if it migrates across one location twice (i.e. sea-level fall, then sea-level rise, then sea-level fall; Fig. 2). While the sea-level hinge line does not necessarily follow the solid earth hinge line exactly, it may be strongly influenced by it (Fig. 2C,D).

The simulated evolution of the sea-level hinge lines reflects similar characteristics to the solid earth hinge lines from previous models, but with some variability following collapse of the Fennoscandian ice sheet due to small fluctuations of the Greenland and Antarctic ice sheets (Fig. 6A). The relationship between earth structure and hinge line reversals remains the same: the sea-level hinge line only reverses migration direction

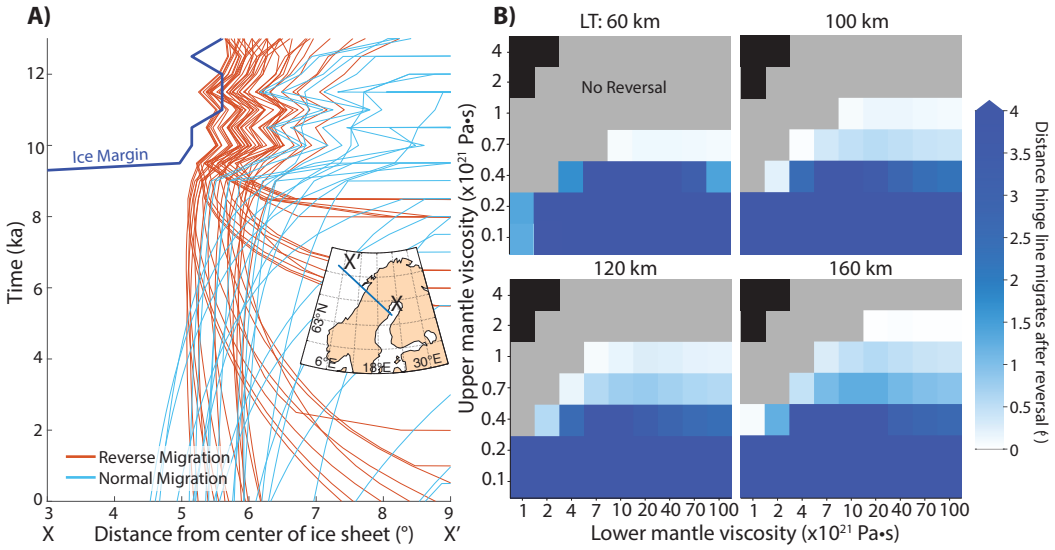

Figure 5: **As in Figure 4, but for LN-NO model predictions for the evolution of the solid earth hinge line across Scandinavia (transect X-X').** The model includes no ocean and only the ICE7G Eurasian ice sheet complex. See Figure 4 for detailed plot descriptions and Figures S3 and S4 for versions that include gravitational effects and all ice sheets, respectively.

if mantle viscosity increases with depth and the amount of reverse migration is controlled by the viscosity contrast (Fig. 6). The exception to this relationship is seen for high upper mantle viscosities and is related to the influence of distant ice sheets as described in the previous section and in the supplement (Fig. S4).

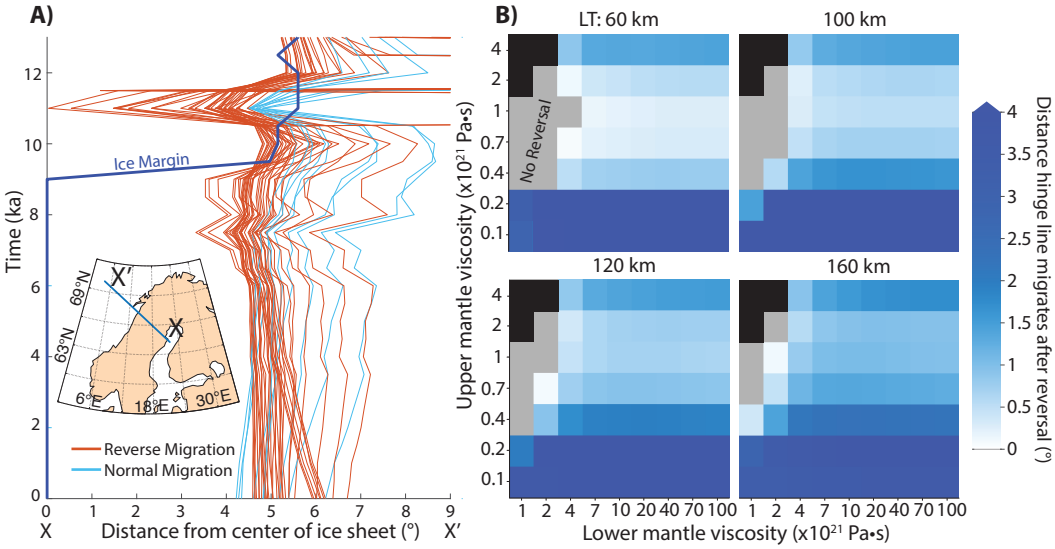

Figure 6: **As in Figure 5, but for LN-SL model predictions for the evolution of the sea-level hinge line across Scandinavia.** The model includes a gravitationally self-consistent ocean and is forced with the ICE7G ice model. See Figure 4 for detailed plot descriptions. Note, the large excursions around 11 ka are related to the Younger Dryas ice growth (mainly of the LIS) in the ICE7G reconstruction.

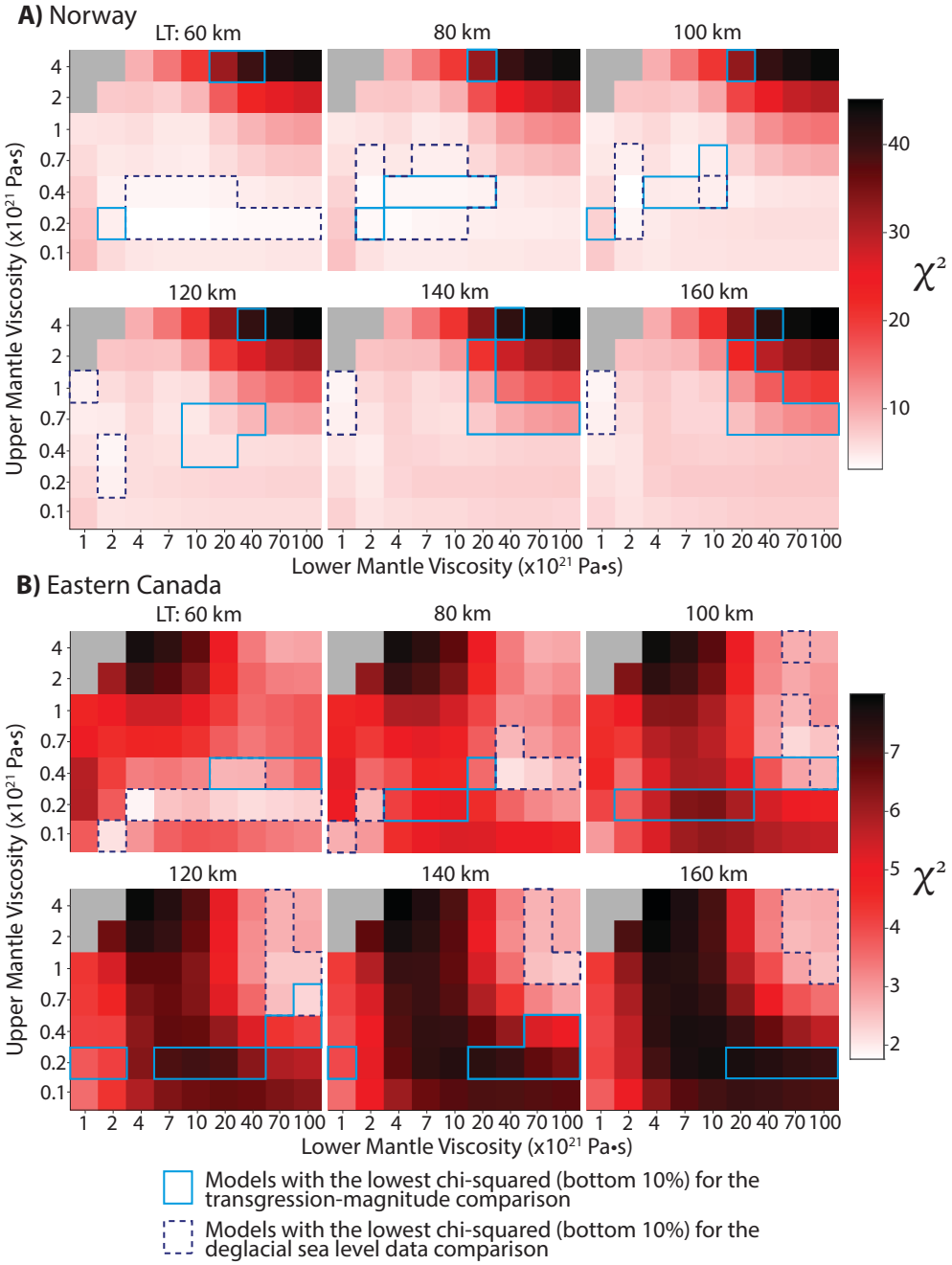

Figure 7: **Chi-squared distributions for the comparison between RSL predictions from the LN-SL experiment and the sea-level data in (A) Norway (Creel et al., 2022) and (B) Eastern Canada Vacchi et al. (2018)**. Each box represents one GIA model; color bar indicates corresponding chi-squared values. Dashed blue contour line indicates models with chi-squared values in the bottom ten percent. Solid light blue contour indicates the same but for the transgression-magnitude comparison (see Fig. 8). Gray squares indicate unrealistic parameter combinations (decreasing viscosity with depth in the mantle) for which GIA models were not run.

3.2. Data-model misfit result

In both Norway (Fig. 7A) and Eastern Canada (Fig. 7B), the misfit between the LN-SL simulation predictions and postglacial sea-level data is sensitive to the contrast between mantle viscosity and lithospheric

thickness (Fig. 7; Fig. S3). In Norway, best-fitting simulations cluster around thinner lithospheres (60-100 km), upper mantle viscosities of $0.2-0.4*10^{21}$ Pa s, and lower mantle viscosities of $2-7*10^{21}$ Pa s. In Eastern Canada, the best fitting simulations fall into two distinct regions of the parameter space; simulations with a thin lithosphere (60 km) cluster around $0.2*10^{21}$ Pa s upper mantle viscosity and a range of lower mantle viscosities. With increasing lithospheric thickness, the region of low misfit moves towards higher upper mantle viscosities ($0.7-4*10^{21}$ Pa s) and higher lower mantle viscosities ($70-100*10^{21}$ Pa s). Of the best fitting 10% of simulations in both regions, viscosity in almost all increases across the transition zone (Fig. 7).

Similar comparisons using the PAT-7G and ANU-7G ice models (see Supplemental Fig. S5 and Section 2.2) demonstrate that chi-squared values are also sensitive to the ice sheet, particularly in Norway where RSL predictions from the PAT-7G model fit sea-level data worse than predictions from the ICE7G model (Fig. S5). In North America, the ANU-7G and ICE7G provide similar fit to the sea-level data. In both locations, the representation of the distant ice sheet (e.g., PAT-7G versus ICE7G in Canada) has a minimal effect on the misfit results (Fig. S5).

Results from the goodness-of-fit test between GIA model predictions and STEHM predictions of transgression magnitude also favor a viscosity increase from the upper to the lower mantle (Fig. 8). Simulations with a low viscosity contrast underpredict or do not predict the transgression, while a high contrast tends to overpredict the transgression magnitude. The best fitting simulations for Norway cluster around a lithospheric thickness of 120-160 km and upper and lower mantle viscosities of $0.7*10^{21}$ and $10-70*10^{21}$ Pa s, respectively. The best fitting simulations for Eastern Canada cluster around a lithospheric thickness of 80-100 km and upper and lower mantle viscosities of $0.2-0.4*10^{21}$ and $4-100*10^{21}$ Pa s. In both regions, the best-fitting simulations include viscosities that increase across the transition zone (Fig. 8).

Results from the transgression magnitude goodness-of-fit test also vary with ice sheet reconstruction (Fig. S6). In Norway, the PAT-7G model produces an overall worse fit for all solid earth structures. The ANU-7G model provides similar misfit values to the ICE7G model for thin lithospheres (60-80 km) but shows a slightly poorer fit for thicker lithospheres (100-140 km). In Eastern Canada, the ANU-7G produces similarly minimal misfit to the ICE7G model, but with a preference for higher viscosities ($0.4-0.7*10^{21}$ Pa s) in the upper mantle. The representation of the distant Eurasian ice history (PAT-7G versus ICE7G) has minimal effect on the misfit results in Canada.

While based on the same datasets, the two misfit tests performed here target different time periods and types of observations, so we expect that they probe different parts of the mantle and can therefore be combined for a more informative constraint on mantle viscosity. In both tests, the best fitting simulations (blue outlines in Fig. 7 and 8) overlap for some earth structures. In Norway, these cluster around a lithospheric thickness of 80 km, an upper mantle viscosity of $0.4*10^{21}$ Pa s, and lower mantle viscosities of $2-10*10^{21}$ Pa s. In Eastern Canada, the only three simulations that overlap cluster around lithospheric thicknesses of 60-100 km, an upper mantle viscosity of $0.4*10^{21}$ Pa s and lower mantle viscosities of $10-100*10^{21}$ Pa s (Fig. 7 and 8).

The predicted transgression magnitude for the absolute best fitting simulations in the STEHM goodness-of-fit test are shown in Figures 9 and 10. In both regions, the best-fitting models capture the spatial pattern and the magnitude of the STEHM predictions. In Scandinavia, the GIA model predicted transgression extends from the Barents Sea to the North Sea, intersecting the Norwegian coastline everywhere except in the central region and along the east-facing coast (Fig. 9). Similar to the STEHM, the GIA model predicts increasing magnitude with distance from the mainland. Where the GIA predictions deviate significantly from the STEM model tends to be far from the coastline where there is limited sea-level data to inform the STEHM (Creel et al., 2022). The GIA model predicted high stand age in Norway (ranging in most locations from 7-5 ka) matches the general range predicted by the STEHM (Creel et al., 2022), although in specific locations, particularly southern Norway, the GIA model underpredicts the age by up to a few thousand years. In Eastern Canada, the GIA model predicts a transgression in four of the six locations where the STEHM predicts a transgression based on direct sea-level evidence. The GIA model also predicts much younger high stand ages for Eastern Canada (3-5 ka in most regions) compared to Norway, which is in line with the timing supported by the STEHM and direct sea-level observations (Dionne, 1988; Vacchi et al., 2018).

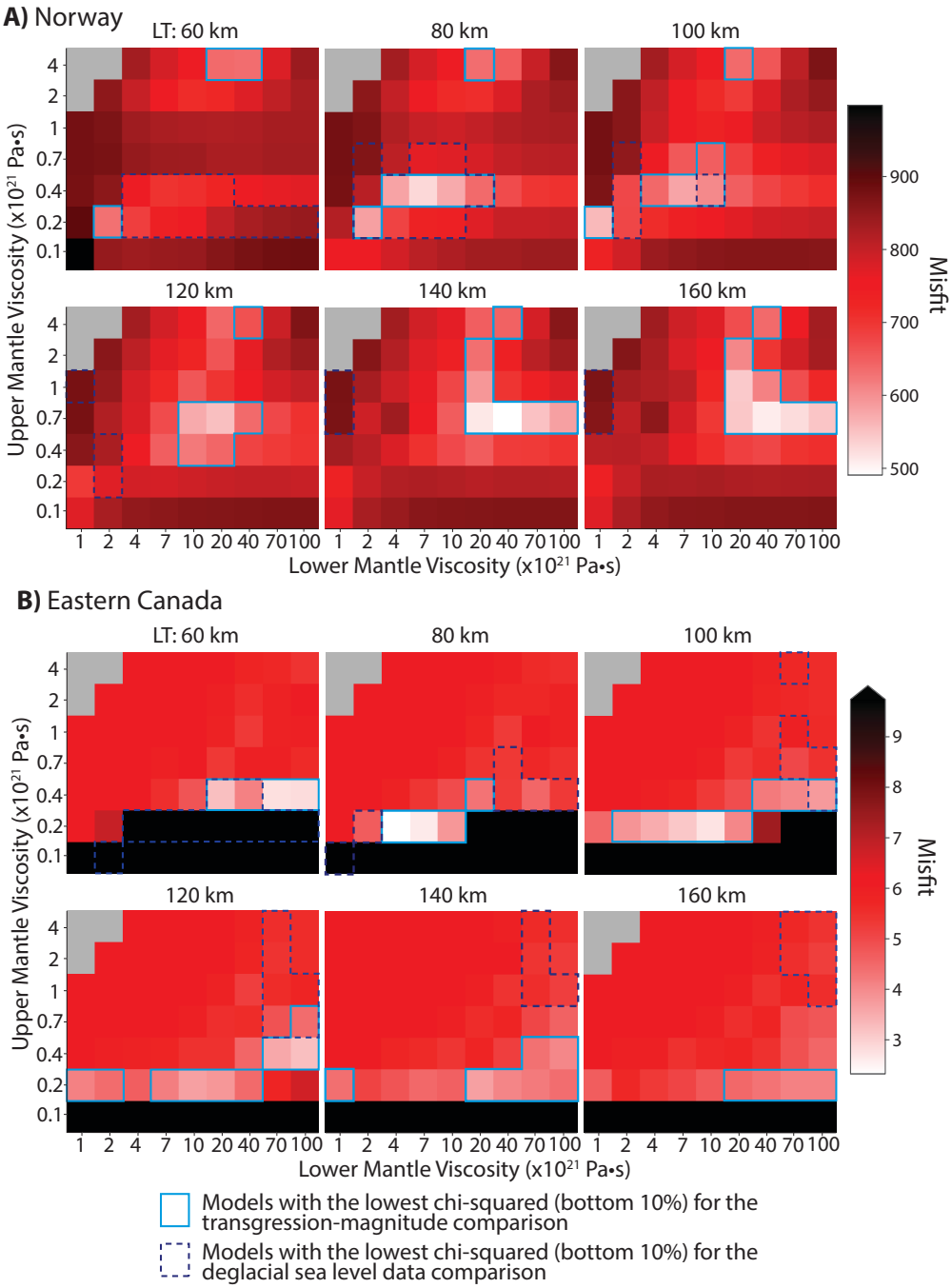

Figure 8: **GIA model (LN-SL - ICE7G) misfit for the goodness-of-fit test to the STEHMs of transgression magnitude in (A) Norway (B) Eastern Canada.** See Figure 7 for further details.

4. Discussion

4.1. Reverse migration mechanics

In a viscosity-stratified mantle, the amount of surface displacement is linked to the competing rates of deformation between layers with different viscosities. Results from the NM-NO model (Fig. 3B) show

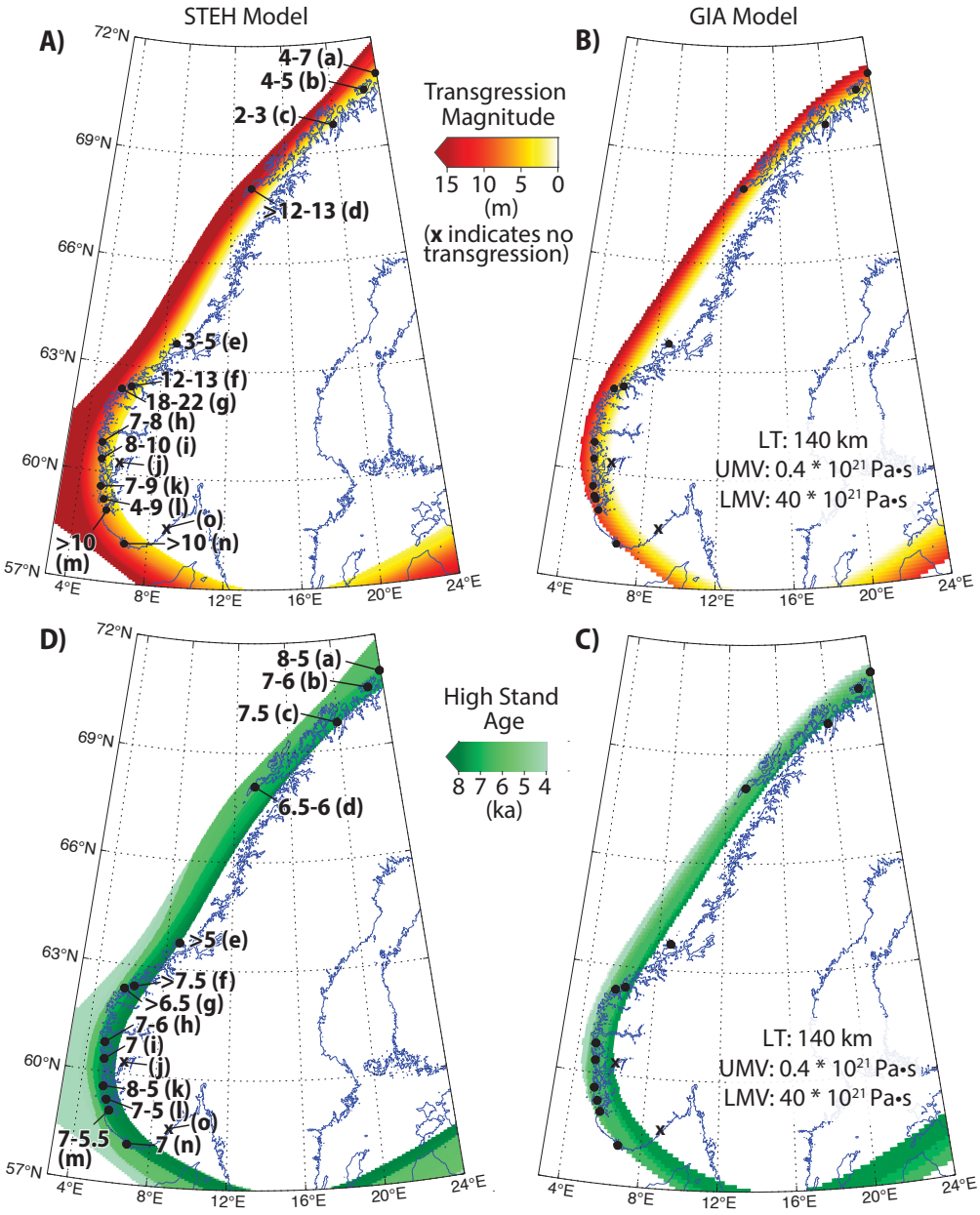

Figure 9: **Transgression magnitude in Norway for (A) the GIA simulation that best fits observed Holocene transgression magnitude and (B) STEHM of Creel et al. (2022).** The high stand ages for these models are shown in C and D. The best fitting GIA simulation has a lithospheric thickness of 140 km and upper and lower mantle viscosities of $0.4 * 10^{21}$ and $40 * 10^{21}$ Pa s, respectively. GIA predictions are linearly interpolated to the higher resolution grid of the STEHM of Creel et al. (2022) for comparison purposes. Black dots indicate transgression observations and their approximate magnitudes following Fjeldskaar and Bondevik (2020): (a, b) Romundset et al. (2011); (c) Rasmussen et al. (2018); (d) Moller (1984); (e) Kjemperud (1986); (f) Svendsen and Mangerud (1987); (g) Bondevik et al. (1998); (h) Kaland (1984); (i) Lohne et al. (2007) and references therein; (j) Romundset et al. (2010); (k) Fægri (1943); Kaland (1984); (l, m, n) Prøsch-Danielsen (2006) and references therein; (o) Romundset et al. (2018) .

how these competing rates can produce reverse migration. During deglaciation, the upper mantle relaxes towards equilibrium faster than the lower mantle due to its lower viscosity. Both the uplifting region and the

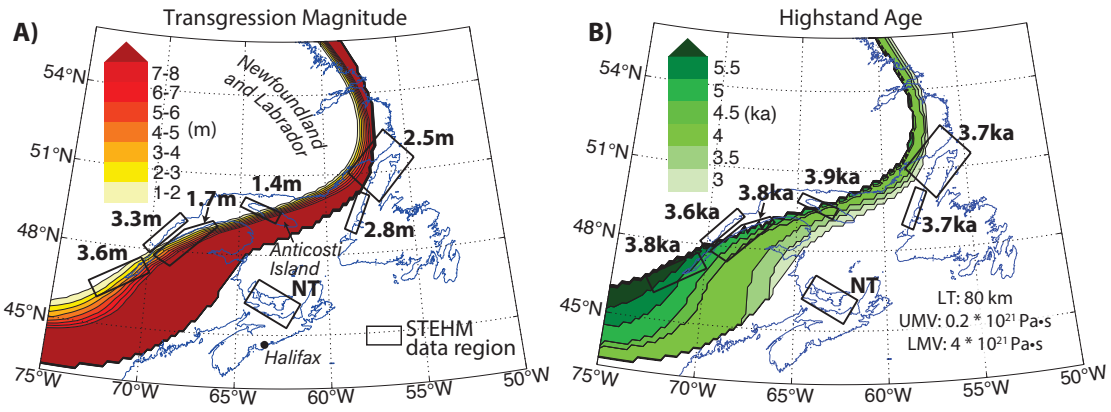

Figure 10: **Predicted transgression magnitude in Eastern Canada (A) and high stand age (B) for the GIA simulation that best fits the STEHM predicted transgression magnitudes.** The best fitting simulation has a lithospheric thickness of 80 km and upper and lower mantle viscosities of $0.2 * 10^{21}$ and $4 * 10^{21}$ Pa s, respectively. Boxes indicate data regions and are labeled with the corresponding transgression magnitudes (A) and high stand ages (B) from the STEHM reported in Vacchi et al. (2018).

subsiding peripheral bulge migrate towards the retreating ice front. Concurrently, the lower mantle responds to ice melt more slowly and thus maintains a larger region of uplift than the upper mantle over time. Consequently, an intermediate zone emerges where upper mantle material is subsiding and lower mantle material is uplifting (Fig 3B, inset 1). Though the rate of deformation is initially stronger in the upper mantle, over time upper mantle subsidence slows and is surpassed by lower mantle uplift. This behavior causes the region of surface uplift to expand and generates reverse migration (Fig 3B, inset 2). Thus, reverse migration can be thought of as a natural consequence of competing rates of deformation between layers of Earth's mantle with different viscosities. While this study focuses on a two-layered mantle, it is reasonable to assume that any earth structures whose viscosities increase sufficiently with depth may lead to the same effect. An interesting prediction from this mechanism is that as the region of uplift in the lower mantle continues to shrink into the future, the hinge line may again change direction and migrate back towards the former ice mass. However, at that point the rates of uplift and subsidence will likely be small and possibly undetectable. It is also worth noting that horizontal motions are affected by the mantle dynamics discussed here (Hermans et al., 2018), but are not the focus of this study.

A few modeling studies have predicted reverse migration, but none have linked the process to direct observations of sea-level change. Cathles (1980) and Fjeldskaar (1994) present models that show the sea-level hinge line ('zero-isobase') and peripheral bulge maximum moving away from the ice load during the late deglaciation, however, both argue that a stationary or nearly stationary isobase best fits observations from Fennoscandia. Neither study explores the solid earth processes that drive reverse migration in their models.

4.2. The role of reverse migration and GMSL rise in generating transgressions

Our results support the hypothesis that solid earth deformation, specifically reverse migration, was the primary driver of near-field Holocene transgressions in Eastern Canada and Norway. While the models do not perfectly predict the transgression everywhere on the coastline, they capture the general spatio-temporal trends and, importantly, do so only for models that include reverse migration. In models without reverse migration, the rate of GMSL rise is not sufficient to out-compete uplift and generate a transgression. Still, concurrent GMSL change certainly modulated the specific spatio-temporal patterns of the transgression. In Norway, for example, the transgression is restricted to the Early Holocene when concurrent GMSL rise amplified the transgression. In Canada, the transgression occurred between ~8 ka and ~4 ka (Vacchi et al., 2018), after GMSL rise had slowed (Lambeck et al., 2014; Bradley et al., 2016) or stopped (Roy and Peltier, 2017), which may explain the smaller transgression magnitude there.

4.3. Mantle viscosity constraints

The preferred earth structures for Norway and Canada for both tests generally agree with previously published estimates. Using RSL data from the US East Coast, just south of the RSL data from Vacchi et al. (2018), Roy and Peltier (2015) associated the ICE-6G_C ice model with a best fitting Earth model (VM6) composed of a 90 km thick lithosphere, 0.45 * 10^{21} Pa s upper mantle viscosity and lower mantle viscosity increasing from 0.9 to 8 * 10^{21} Pa s with depth. The ICE7G model used here (Roy and Peltier, 2017) is associated with the VM7 radial earth structure which resembles VM6 save that its lower mantle increases more continuously with depth (Roy and Peltier, 2017). By contrast, the earth structure associated with the ANU LIS (Lambeck et al., 2017) has a lithospheric thickness of 102 km (85-120, 95% confidence interval), upper mantle viscosity of 0.51 $*10^{21}$ Pa s (3.5-7.5$*10^{21}$, 95% CI) and lower mantle viscosity of 13 $*10^{21}$ Pa s (8-28$*10^{21}$, 95% CI). Our results are consistent with these earth structures but tend toward slightly weaker upper mantle viscosities (Fig. 7 and 8).

In Norway, Steffen and Kaufmann (2005) found that RSL and GPS data were best fit by an Earth model with lithospheric thickness of 120 km, upper mantle viscosity of $4 * 10^{21}$ Pa s and lower mantle viscosity of $100 * 10^{21}$ Pa s, although they note that the lithospheric thickness and lower mantle viscosity are poorly constrained. These values support the results from the best-fitting regions in our misfit tests (Fig. 7 and 8). Fjeldskaar and Bondevik (2020) determined that the Norwegian Tapes Transgression was best fit using an earth structure with an 80 km lithosphere, a 75 km asthenosphere with a viscosity of 0.013 * 10^{21} Pa s, and a mantle below that of uniform 10^{21} Pa s viscosity. This differs notably from our results that indicate a contrast in viscosity between the upper and lower mantle is necessary to simulate the transgression. It is possible that the small but very low viscosity asthenosphere has a comparable influence on the mantle dynamics. Regardless, it is challenging to compare to their model results as the authors use a flat-Earth GIA approximation that did not solve the gravitationally self-consistent sea-level equation.

The sensitivity of the predicted transgressions to mantle viscosity stratification demonstrates their potential to constrain the vertical structure of Earth's interior. There is agreement that mantle viscosity increases with depth below the lithosphere. However, the depth at which this increase occurs on average is not well-constrained (Rudolph et al., 2015; Lau et al., 2016). Our findings suggest that in the vicinity of Holocene transgressions, the local mantle structure includes a viscosity increase at 670 km. As discussed above, this viscosity increase may not necessarily be stepwise as implemented in out models, but rather continuous or include multiple discontinuities. It also likely varies laterally. Regardless, the connection between reverse migration and Holocene transgressions implies that there is an ($\sim$ order of magnitude) increase in viscosity above 1000 km depth in these locations, since it is generally understood that Pleistocene ice sheets are only sensitive to such depths (Mitrovica and Peltier, 1992).

4.4. Remaining challenges in modeling transgressions

Even the best-fitting Earth parameters do not reproduce the transgressions constraints or the postglacial sea-level datasets perfectly. This is to be expected given our assumption of a 1-D earth structure. Laterally varying mantle viscosity, lithospheric thickness, and transition zone depth could explain some of this misfit and reconcile the disagreement between models that fit the deglacial sea-level data and those that fit the transgression magnitude. Nevertheless, our results narrow the parameter space for future 3D GIA modeling. Even in the context of 1D models, the three-layer structure may be overly simple: 1D models with continuously varying viscosity with depth (see section **??**) could reduce data-model misfit. Ice sheet reconstruction uncertainties present a further challenge in fitting both the entire postglacial sea-level datasets and the transgressions magnitude constrains. We find that ice model choice primarily affects the spatial pattern of transgressions rather than their magnitude; future work can leverage this finding to examine the likelihood of various ice sheet geometries.

Some RSL data may record processes other than GIA, namely tectonic deformation. This has been addressed in tectonically active regions such as the west coast of North America where a small near-field transgression and high stand is observed (Shugar et al., 2014), but is also possibly a relevant process in some locations of tectonically 'stable' margins like Norway (Fjeldskaar et al., 2000). If tectonics did influence post-glacial RSL in Norway, it likely had a local or regional effect rather than a long wavelength, spatially coherent signal like the Tapes transgression (Creel et al., 2022).

Another challenge in linking model results to observations is the narrow area over which the transgression occurs. On Anticosti Island, Canada, for example, the model predicts a range of magnitudes from zero to over eight meters (Fig. 11). The sparse data in this location (Vacchi et al., 2018) cannot capture these gradients and thus provide a poor (coarse) constraint on the model. Such strong gradients over a small region highlight the importance of having a high density of RSL data to better constrain the GIA model inputs.

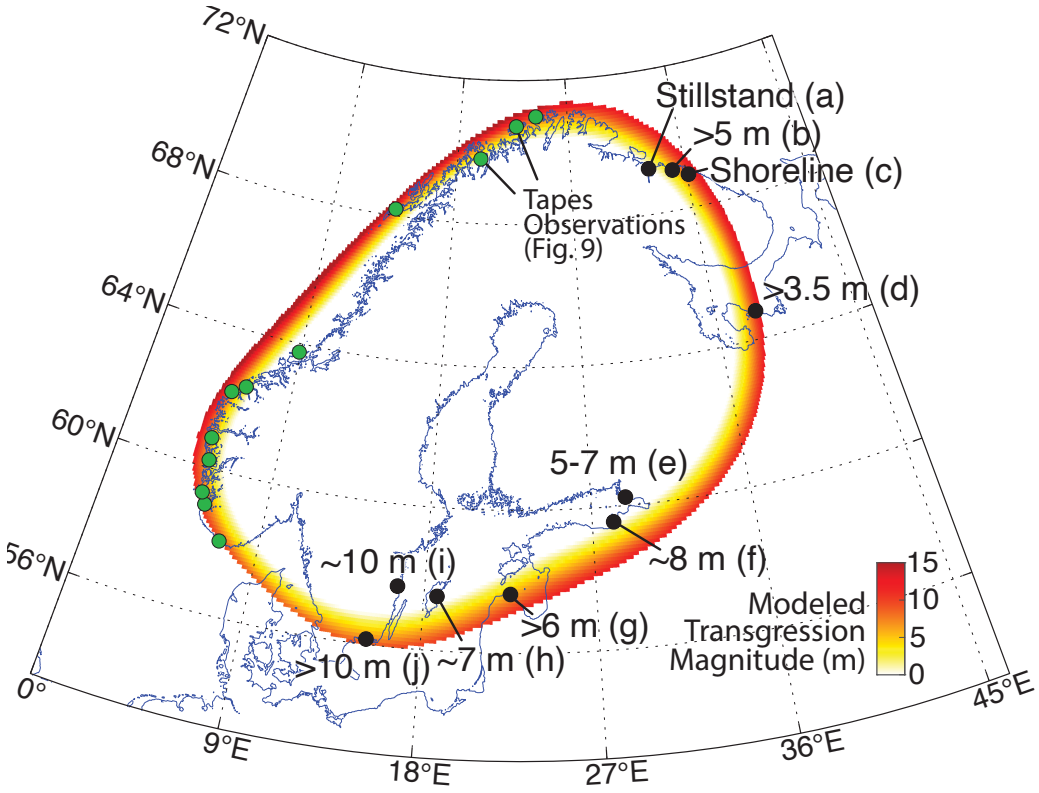

Figure 11: **Holocene transgression magnitude from the GIA model that best fits the STEHM transgression of Creel et al. (2022).** The GIA model includes the ICE7G ice history, 140 km lithospheric thickness, $0.4 * 10^{21}$ Pa s upper mantle viscosity, and $40 * 10^{21}$ Pa s lower mantle viscosity. Black markers and numbers denote location and approximate magnitudes of Holocene transgressions in Northern Europe: (a) Corner et al. (2001); (b) Kolka et al. (2023); (c) Snyder et al. (1996); (d) Kublitskiy et al. (2023); (e) Miettinen et al. (2007); (f) Rosentau et al. (2013); (g) Rosentau et al. (2023); (h) Strandberg et al. (2020); (i) Katrantsiotis et al. (2022); (j) Yu et al. (2007). Green markers indicate locations with evidence for the Tapes Transgression following Fjeldskaar and Bondevik (2020) (as in Fig. 9). GIA model predictions were linearly interpolated to higher spatial resolution for interpretation.

4.5. Implications for near-field Holocene transgressions

Our results can shed light on Holocene transgressions elsewhere, including in the British Isles, Canadian Arctic, British Columbia, Svalbard, Russian Arctic, East Antarctica, and across the Baltic Sea (Zwartz et al., 1998; Forman, 2004; Nixon; Shennan et al., 2018; Rosentau et al., 2021; Kublitskiy et al., 2023; Letham et al., 2024). In contrast to the standard view that such transgressions are solely the result of GMSL temporarily outpacing isostatic uplift, we argue—by extension of our results from Eastern Canada and Norway—that they are also influenced by reverse migration. In Northern Europe, for example, the Norwegian Tapes Transgression coincides with transgressions in the Baltic Sea (sometimes called the 'Littorina' or 'Litorina' Transgression), in the White Sea, and along the Kola Peninsula (Miettinen et al., 2007; Yu et al., 2007; Rosentau et al., 2021). The best fitting GIA model for the Tapes Transgression also predicts a transgression

across the Kola peninsula and Baltic and White Seas (Fig. 11). While there are discrepancies between LN-SL model predictions and sea-level reconstructions in these regions due potentially to the model limitations outlined in section 4.5, the simulation produces a transgression around the entire FIS that is of similar magnitude and timing to the observations. We also note that models with no Norwegian transgression also produce no transgression around the Baltic.

Additional factors may be important when considering Holocene transgressions in regions beyond Eastern Canada and Norway. The Celtic Ice Sheet, for example, was roughly a third the size of the FIS and caused less isostatic uplift following deglaciation, which may have allowed GMSL rise to more readily outcompete GIA-related RSL fall (Patton et al., 2017). Proximity to larger ice masses likely also influences solid Earth dynamics below the smaller ice sheet. The Celtic and Cordilleran Ice Sheets existed adjacent to the much larger FIS and LIS, respectively, and could have been affected by the collapsing peripheral bulges of their larger neighbors (Shennan et al., 2018) complicating the reverse migration process.

Deglaciation pattern is also important to consider. The Holocene transgression in Svalbard, for example, was shaped by the retreat of the Barents-Kara Ice Sheet to surrounding archipelagos following the collapse of its central marine-based sector—a different pattern from the FIS and LIS retreat histories (Patton et al., 2017). Around the East Antarctic Ice Sheet, the Holocene transgression identified by (Zwartz et al., 1998) is challenging to interpret due to the overlapping effects of postglacial GIA and contemporary Antarctic ice mass changes.

5. Conclusion

Our GIA modeling experiments isolate a pattern of solid earth deformation we term 'reverse migration', in which the inner margin of the peripheral bulge migrates first toward and then away from the center of former ice loading. We show that reverse migration is caused by a viscosity contrast between Earth's upper and lower mantle. Comparing modeling predictions to geologic observations of the transgression in Norway and Eastern Canada, we show that models with this viscosity contrast simulate reverse migration and fit the record of Holocene transgressions. This provides a useful complementary constraint on regional mantle viscosity. Our result supports the hypothesis that near-field Holocene transgressions relate to solid earth deformation and are not solely caused by GMSL outpacing isostatic uplift. We suggest that reverse migration can also help explain observations from other formerly glaciated regions, including around the Scandinavian Peninsula, the British Isles, Svalbard, and the North American West Coast.

Code Availability

A version of the code used for the LN-SL and LN-NO models is available at: `https://github.com/jaustermann/SLcode`.

Data Availability

Sea level data used in this study is published in Vacchi et al. (2018) and Creel et al. (2022).

Author contributions

Conceptualization: SC, JA, WD. Methodology: SC, JA. Formal Analysis, Investigation, Visualization, Writing – original draft: SC. Software: JA, AL. Data curation: SC, RC. Supervision: JA, WD. Writing – review & editing: All co-authors.

Declaration of competing interest

The authors declare that they have no known competing financial interests or personal relationships that could have appeared to influence the work reported in this paper.

Acknowledgements

This work was supported by NASA award 80NSSC21K1790 (SC, JA). We thank James Davis and Roger Buck for helpful discussions. We acknowledge computing resources from Columbia University's Shared Research Computing Facility project, which is supported by NIH Research Facility Improvement Grant 1G20RR030893-01, and associated funds from the New York State Empire State Development, Division of Science Technology and Innovation (NYSTAR) Contract C090171, both awarded April 15, 2010. The authors acknowledge PALSEA, a working group of the International Union for Quaternary Sciences (INQUA) and Past Global Changes (PAGES), which in turn received support from the Swiss Academy of Sciences and the Chinese Academy of Sciences. Figures 1, 8, 9, and 10 were created using M_Map (Pawlowicz, 2020). Coastlines in Figures 8, 9, and 10 were created using the Generic Mapping Tools (GMT; Wessel et al., 2019).

Appendix A. Disc Ice Model

The radially symmetric disc-shaped ice load was constructed to generally match the timing and magnitude of the Laurentide Ice Sheet deglaciation. A glaciation phase lasting 39 kyrs was constructed by linearly interpolating over space and time at 500-year intervals between a very small initial ice sheet at 60 ka, $H_{ice}(r, t = 60)$, and the glacial maximum ice sheet at 21 ka, $H_{ice}(r, t = 21)$, defined as:

$$H_{ice}(r, t = 60\text{ka}) = \left[\frac{H_{max} - (r\sqrt{H_{max}})}{(R_{max} - 12)^2}\right]\left[\frac{1}{13}\right] \tag{A.1}$$

$$H_{ice}(r, t = 21\text{ka}) = \left[\frac{H_{max} - (r\sqrt{H_{max}})}{(R_{max})^2}\right] \tag{A.2}$$

Where t is time in ka, r is the radial distance from the south pole in great circle degrees, H_{max} is the maximum thickness, 3000 meters, and R_{max} is the maximum radius, 15 degrees. The ice geometries were linearly interpolated onto a lat-lon grid. The small initial ice mass is necessary for numerical reasons in the NM-NO model.

For the deglacial period (21 ka to present), the ice thickness is given by the following equation:

$$H_{ice}(r, t) = \left[\frac{H_{max} - (r\sqrt{H_{max}})}{(R_{max} - 0.5(21 - t))^2}\right]\left[\frac{t - 8}{21 - 8}\right] \text{ for } 21 \geq t \geq 8 \tag{A.3}$$

Ice thickness was calculated at 500-year intervals and interpolated onto a lat-lon grid.

References

Al-Attar, D., Tromp, J., 2014. Sensitivity kernels for viscoelastic loading based on adjoint methods. Geophysical Journal International 196, 34–77. URL: http://academic.oup.com/gji/article/196/1/34/593319/Sensitivity-kernels-for-viscoelastic-loading-based, doi:10.1093/gji/ggt395.

Amante, C., Eakins, B., 2009. ETOPO1 arc-minute global relief model : procedures, data sources and analysis. URL: https://repository.library.noaa.gov/view/noaa/1163.

Auriac, A., Whitehouse, P.L., Bentley, M.J., Patton, H., Lloyd, J.M., Hubbard, A., 2016. Glacial isostatic adjustment associated with the Barents Sea ice sheet: A modelling inter-comparison. Quaternary Science Reviews 147, 122–135. URL: https://www.sciencedirect.com/science/article/pii/S0277379116300439, doi:10.1016/j.quascirev.2016.02.011.

Austermann, J., Mitrovica, J.X., Latychev, K., Milne, G.A., 2013. Barbados-based estimate of ice volume at Last Glacial Maximum affected by subducted plate. Nature Geoscience 6, 553–557. URL: http://www.nature.com/articles/ngeo1859, doi:10.1038/ngeo1859.

Baril, A., Garrett, E., Milne, G., Gehrels, W., Kelley, J., 2023. Postglacial relative sea-level changes in the Gulf of Maine, USA: Database compilation, assessment and modelling. Quaternary Science Reviews 306, 108027. URL: https://linkinghub.elsevier.com/retrieve/pii/S0277379123000756, doi:10.1016/j.quascirev.2023.108027.

Barnhardt, W.A., Roland Gehrels, W., Kelley, J.T., 1995. Late Quaternary relative sea-level change in the western Gulf of Maine: Evidence for a migrating glacial forebulge. Geology 23, 317. URL: https://pubs.geoscienceworld.org/geology/article/23/4/317-320/206267, doi:10.1130/0091-7613(1995)023<0317:LQRSLC>2.3.CO;2.

Bondevik, S., Svendsen, J., Mangerud, J., 1998. Distinction between the Storegga tsunami and the Holocene marine transgression in coastal basin deposits of western Norway. Journal of Quaternary Science 13, 529–537. doi:10.1002/(SICI)1099-1417(1998110)13:6<529::AID-JQS388>3.0.CO;2-1.

Borreggine, M., Powell, E., Pico, T., Mitrovica, J.X., Meadow, R., Tryon, C., 2022. Not a bathtub: A consideration of sea-level physics for archaeological models of human migration. Journal of Archaeological Science 137, 105507. URL: https://linkinghub.elsevier.com/retrieve/pii/S0305440321001771, doi:10.1016/j.jas.2021.105507.

Bradley, S.L., Milne, G.A., Horton, B.P., Zong, Y., 2016. Modelling sea level data from China and Malay-Thailand to estimate Holocene ice-volume equivalent sea level change. Quaternary Science Reviews 137, 54–68. URL: https://linkinghub.elsevier.com/retrieve/pii/S0277379116300348, doi:10.1016/j.quascirev.2016.02.002.

Cathles, L.M., 1980. Interpretation of postglacial isostatic adjustment phenomena in terms of mantle rheology. Earth Rheology, Isostasy and Eustasy , 11–45Publisher: Wiley New York.

Clark, J.A., Farrell, W.E., Peltier, W., 1978. Global Changes in Postglacial Sea Level: A Numerical Calculation. Quaternary Research 9, 265–287. doi:10.1016/0033-5894(78)90033-9.

Corner, G.D., Kolka, V.V., Yevzerov, V.Y., Møller, J.J., 2001. Postglacial relative sea-level change and stratigraphy of raised coastal basins on Kola Peninsula, northwest Russia. Global and Planetary Change 31, 155–177. URL: https://linkinghub.elsevier.com/retrieve/pii/S0921818101001187, doi:10.1016/S0921-8181(01)00118-7.

Crawford, O., Al-Attar, D., Tromp, J., Mitrovica, J.X., Austermann, J., Lau, H.C.P., 2018. Quantifying the sensitivity of post-glacial sea level change to laterally varying viscosity. Geophysical Journal International 214, 1324–1363. URL: https://academic.oup.com/gji/article/214/2/1324/4993542, doi:10.1093/gji/ggy184.

Creel, R., Austermann, J., Kopp, R., Khan, N., Albrecht, T., Kingslake, J., 2023. Global mean sea level higher than present during the Holocene. preprint. Earth Sciences. URL: https://eartharxiv.org/repository/view/5419/, doi:10.31223/X5JT11.

Creel, R.C., Austermann, J., Khan, N.S., D'Andrea, W.J., Balascio, N., Dyer, B., Ashe, E., Menke, W., 2022. Postglacial relative sea level change in Norway. Quaternary Science Reviews 282, 107422. URL: https://linkinghub.elsevier.com/retrieve/pii/S0277379122000531, doi:10.1016/j.quascirev.2022.107422.

Dalca, A.V., Ferrier, K.L., Mitrovica, J.X., Perron, J.T., Milne, G.A., Creveling, J.R., 2013. On postglacial sea level—III. Incorporating sediment redistribution. Geophysical Journal International 194, 45–60. URL: http://academic.oup.com/gji/article/194/1/45/644503/On-postglacial-sea-levelIII-Incorporating-sediment, doi:10.1093/gji/ggt089.

Davis, J.L., Mitrovica, J.X., 1996. Glacial isostatic adjustment and the anomalous tide gauge record of eastern North America 379.

Dionne, J.C., 1988. Holocene Relative Sea-Level Fluctuations in the St. Lawrence Estuary, Québec, Canada. Quaternary Research 29, 233–244. doi:10.1016/0033-5894(88)90032-4.

Dziewonski, A.M., Anderson, D.L., 1981. Preliminary reference Earth model. Physics of the Earth and Planetary Interiors 25, 297–356. URL: https://www.sciencedirect.com/science/article/pii/0031920181900467, doi:10.1016/0031-9201(81)90046-7.

Engelhart, S.E., Horton, B.P., 2012. Holocene sea level database for the Atlantic coast of the United States. Quaternary Science Reviews 54, 12–25. URL: https://linkinghub.elsevier.com/retrieve/pii/S0277379111002927, doi:10.1016/j.quascirev.2011.09.013.

Engelhart, S.E., Vacchi, M., Horton, B.P., Nelson, A.R., Kopp, R.E., 2015. A sea-level database for the Pacific coast of central North America. Quaternary Science Reviews 113, 78–92. URL: https://linkinghub.elsevier.com/retrieve/pii/S0277379114004843, doi:10.1016/j.quascirev.2014.12.001.

Farrell, W.E., Clark, J.A., 1976. On Postglacial Sea Level. Geophysical Journal of the Royal Astronomical Society 46, 647–667.

Fjeldskaar, W., 1994. The amplitude and decay of the glacial forebulge in Fennoscandia. NORSK GEOLOGISK TIDSSKRIFT vol. 74, 2–8.

Fjeldskaar, W., Bondevik, S., 2020. The Early-Mid Holocene transgression (Tapes) at the Norwegian coast – comparing

observations with numerical modelling. Quaternary Science Reviews 242, 106435. URL: https://linkinghub.elsevier.com/retrieve/pii/S0277379120303978, doi:10.1016/j.quascirev.2020.106435.

Fjeldskaar, W., Lindholm, C., Dehls, J.F., Fjeldskaar, I., 2000. Postglacial uplift, neotectonics and seismicity in Fennoscandia. Quaternary Science Reviews 19, 1413–1422. URL: https://www.sciencedirect.com/science/article/pii/S0277379100000706, doi:10.1016/S0277-3791(00)00070-6.

Forman, S., 2004. A review of postglacial emergence on Svalbard, Franz Josef Land and Novaya Zemlya, northern Eurasia. Quaternary Science Reviews 23, 1391–1434. URL: https://linkinghub.elsevier.com/retrieve/pii/S027737910300341X, doi:10.1016/j.quascirev.2003.12.007.

Fægri, K., 1943. Studies on the Pleistocene of Western Norway: III. Bømlo. Arbok Bergens Museums.

Gomez, N., Mitrovica, J.X., Huybers, P., Clark, P.U., 2010. Sea level as a stabilizing factor for marine-ice-sheet grounding lines. Nature Geoscience 3, 850–853. URL: https://www.nature.com/articles/ngeo1012, doi:10.1038/ngeo1012.

Hermans, T.H.J., Van Der Wal, W., Broerse, T., 2018. Reversal of the Direction of Horizontal Velocities Induced by GIA as a Function of Mantle Viscosity. Geophysical Research Letters 45, 9597–9604. URL: https://agupubs.onlinelibrary.wiley.com/doi/10.1029/2018GL078533, doi:10.1029/2018GL078533.

James, T.S., Hutchinson, I., Vaughn Barrie, J., Conway, K.W., Mathews, D., 2007. Relative Sea-Level Change in the Northern Strait of Georgia, British Columbia*. Géographie physique et Quaternaire 59, 113–127. URL: http://id.erudit.org/iderudit/014750ar, doi:10.7202/014750ar.

Jamieson, T.F., 1882. VI—On the Cause of the Depression and Re-Elevation of the Land During the Glacial Period. Geological Magazine 9, 457–466. doi:10.1017/S0016756800172425.

Kaland, P.E., 1984. Holocene shore displacement and shorelines in Hordaland, western Norway. Boreas 13, 203–242. URL: https://onlinelibrary.wiley.com/doi/10.1111/j.1502-3885.1984.tb00070.x, doi:10.1111/j.1502-3885.1984.tb00070.x.

Katrantsiotis, C., Dahl, M., Palm, V., Rönnby, J., Andrén, T., Andrén, E., 2022. Holocene relative sea level changes in the Västervik-Gamlebyviken region on the southeast coast of Sweden, southern Baltic Sea. Boreas , bor.12605URL: https://onlinelibrary.wiley.com/doi/10.1111/bor.12605, doi:10.1111/bor.12605.

Kendall, R.A., Mitrovica, J.X., Milne, G.A., 2005. On post-glacial sea level - II. Numerical formulation and comparative results on spherically symmetric models. Geophysical Journal International 161, 679–706. URL: https://academic.oup.com/gji/article-lookup/doi/10.1111/j.1365-246X.2005.02553.x, doi:10.1111/j.1365-246X.2005.02553.x.

Khan, N.S., Horton, B.P., Engelhart, S., Rovere, A., Vacchi, M., Ashe, E.L., Törnqvist, T.E., Dutton, A., Hijma, M.P., Shennan, I., 2019. Inception of a global atlas of sea levels since the Last Glacial Maximum. Quaternary Science Reviews 220, 359–371. URL: https://linkinghub.elsevier.com/retrieve/pii/S0277379119306468, doi:10.1016/j.quascirev.2019.07.016.

Kjemperud, A., 1986. Late Weichselian and Holocene shoreline displacement in the Trondheimsfjord area, central Norway. Boreas 15, 61–82. URL: https://onlinelibrary.wiley.com/doi/10.1111/j.1502-3885.1986.tb00744.x, doi:10.1111/j.1502-3885.1986.tb00744.x.

Kolka, V., Tolstobrov, D., Corner, G.D., Korsakova, O., Tolstobrova, A., Vashkov, A., 2023. Isolation basin stratigraphy and Holocene relative sea-level change on the Barents Sea coast at Teriberka, Kola Peninsula, northwestern Russia. The Holocene 33, 1060–1072. URL: http://journals.sagepub.com/doi/10.1177/09596836231176489, doi:10.1177/09596836231176489.

Kublitskiy, Y., Repkina, T., Leontiev, P., Shilova, O., Zaretskaya, N., Gurinov, A., Lugovoy, N., Subetto, D., Yakovleva, A., Nam, S.I., Kim, J.H., Son, Y.J., Peretrukhina, A., 2023. Reconstruction of relative sea-level changes based on a multiproxy study of isolated basins on the Onega Peninsula (the White Sea, northwestern Russia). Quaternary International 644-645, 79–95. URL: https://linkinghub.elsevier.com/retrieve/pii/S1040618222001574, doi:10.1016/j.quaint.2022.04.016.

Kuchar, J., Milne, G., Hubbard, A., Patton, H., Bradley, S., Shennan, I., Edwards, R., 2012. Evaluation of a numerical model of the British–Irish ice sheet using relative sea-level data: implications for the interpretation of trimline observations. Journal of Quaternary Science 27, 597–605. URL: https://onlinelibrary.wiley.com/doi/10.1002/jqs.2552, doi:10.1002/jqs.2552.

Lambeck, K., Purcell, A., Zhao, S., 2017. The North American Late Wisconsin ice sheet and mantle viscosity from glacial rebound analyses. Quaternary Science Reviews 158, 172–210. URL: https://linkinghub.elsevier.com/retrieve/pii/S0277379116306047, doi:10.1016/j.quascirev.2016.11.033.

Lambeck, K., Rouby, H., Purcell, A., Sun, Y., Sambridge, M., 2014. Sea level and global ice volumes from the Last Glacial Maximum to the Holocene. Proceedings of the National Academy of Sciences 111, 15296–15303. URL: https://pnas.org/doi/full/10.1073/pnas.1411762111, doi:10.1073/pnas.1411762111.

Lambeck, K., Woodroffe, C.D., Antonioli, F., Anzidei, M., Gehrels, W.R., Laborel, J., Wright, A.J., 2010. Paleoenvironmental Records, Geophysical Modeling, and Reconstruction of Sea-Level Trends and Variability on Centennial and Longer Timescales. URL: https://onlinelibrary.wiley.com/doi/abs/10.1002/9781444323276.ch4. pages: 61-121 Publisher: John Wiley & Sons, Ltd.

Latychev, K., Mitrovica, J.X., Tamisiea, M.E., Tromp, J., Moucha, R., 2005. Influence of lithospheric thickness variations on 3-D crustal velocities due to glacial isostatic adjustment. Geophysical Research Letters 32. URL: https://onlinelibrary.wiley.com/doi/abs/10.1029/2004GL021454, doi:10.1029/2004GL021454. _eprint: https://onlinelibrary.wiley.com/doi/pdf/10.1029/2004GL021454.

Lau, H.C.P., Mitrovica, J.X., Austermann, J., Crawford, O., Al-Attar, D., Latychev, K., 2016. Inferences of mantle viscosity based on ice age data sets: Radial structure. Journal of Geophysical Research: Solid Earth 121, 6991–7012. URL: https://agupubs.onlinelibrary.wiley.com/doi/10.1002/2016JB013043, doi:10.1002/2016JB013043.

Letham, B., Fedje, D., Hebda, C.F., Dyck, A., Stafford, J., Hutchinson, I., Southon, J., Fedje, B., McLaren, D., 2024. Postglacial relative sea level histories of northern Vancouver Island, Canada. Quaternary Science Reviews 326, 108415. URL: https://linkinghub.elsevier.com/retrieve/pii/S0277379123004638, doi:10.1016/j.quascirev.2023.108415.

Lloyd, A.J., Crawford, O., Al-Attar, D., Austermann, J., Hoggard, M.J., Richards, F.D., Syvret, F., 2023. GIA imaging of

3-D mantle viscosity based on palaeo sea level observations – Part I: Sensitivity kernels for an Earth with laterally varying viscosity. Geophysical Journal International 236, 1139–1171. URL: https://academic.oup.com/gji/article/236/2/1139/7440030, doi:10.1093/gji/ggad455.

Lohne, N.S., Bondevik, S., Mangerud, J., Svendsen, J.I., 2007. Sea-level fluctuations imply that the Younger Dryas ice-sheet expansion in western Norway commenced during the Allerød. Quaternary Science Reviews 26, 2128–2151. URL: https://linkinghub.elsevier.com/retrieve/pii/S0277379107001035, doi:10.1016/j.quascirev.2007.04.008.

Miettinen, A., Savelieva, L., Subetto, D.A., Dzhinoridze, R., Arslanov, K., Hyvärinen, H., 2007. Palaeoenvironment of the Karelian Isthmus, the easternmost part of the Gulf of Finland, during the Litorina Sea stage of the Baltic Sea history. Boreas 36, 441–458. URL: https://onlinelibrary.wiley.com/doi/10.1080/03009480701259284, doi:10.1080/03009480701259284.

Mitrovica, J., Milne, G., 2002. On the origin of late Holocene sea-level highstands within equatorial ocean basins. Quaternary Science Reviews 21, 2179–2190. URL: https://linkinghub.elsevier.com/retrieve/pii/S027737910200080X, doi:10.1016/S0277-3791(02)00080-X.

Mitrovica, J.X., Milne, G.A., 2003. On post-glacial sea level: I. General theory. Geophysical Journal International 154, 253–267. URL: https://academic.oup.com/gji/article-lookup/doi/10.1046/j.1365-246X.2003.01942.x, doi:10.1046/j.1365-246X.2003.01942.x.

Mitrovica, J.X., Peltier, W.R., 1992. A comparison of methods for the inversion of viscoelastic relaxation spectra. Geophysical Journal International 108, 410–414. URL: https://academic.oup.com/gji/article-lookup/doi/10.1111/j.1365-246X.1992.tb04623.x, doi:10.1111/j.1365-246X.1992.tb04623.x.

Moller, J., 1984. Holocene shore displacement at Nappstraumen, Lofoten, north Norway. Norsk Geologisk Tidsskrift 64, 1–5.

Murray-Wallace, C.V., Woodroffe, C.D., 2014. Quaternary Sea-Level Changes: A Global Perspective. Cambridge University Press. Google-Books-ID: l13BAgAAQBAJ.

Møller, Jakob, J.J., 1987. Shoreline relation and prehistoric settlement in northern Norway. Norsk Geografisk Tidsskrift - Norwegian Journal of Geography 41, 45–60. URL: https://doi.org/10.1080/00291958708552171, doi:10.1080/00291958708552171. publisher: Routledge.

Nixon, F.C., . The glacial, sea level, and sea ice histories of Melville and Eglinton islands, western Canadian High Arctic: Last Glacial Maximum to present .

Patton, H., Hubbard, A., Andreassen, K., Auriac, A., Whitehouse, P.L., Stroeven, A.P., Shackleton, C., Winsborrow, M., Heyman, J., Hall, A.M., 2017. Deglaciation of the Eurasian ice sheet complex. Quaternary Science Reviews 169, 148–172. URL: https://linkinghub.elsevier.com/retrieve/pii/S0277379117302068, doi:10.1016/j.quascirev.2017.05.019.

Pawlowicz, R., 2020. M_map: A mapping package for MATLAB. URL: www.eoas.ubc.ca/~rich/map.html.

Peltier, W.R., 1974. The impulse response of a Maxwell Earth. Reviews of Geophysics 12, 649–669. URL: https://agupubs.onlinelibrary.wiley.com/doi/10.1029/RG012i004p00649, doi:10.1029/RG012i004p00649.

Peltier, W.R., Andrews, J.T., 1976. Glacial-Isostatic Adjustment—I. The Forward Problem. Geophysical Journal International 46, 605–646. URL: https://doi.org/10.1111/j.1365-246X.1976.tb01251.x, doi:10.1111/j.1365-246X.1976.tb01251.x.

Phinney, R.A., Burridge, R., 1973. Representation of the Elastic - Gravitational Excitation of a Spherical Earth Model by Generalized Spherical Harmonics. Geophysical Journal International 34, 451–487. URL: https://academic.oup.com/gji/article-lookup/doi/10.1111/j.1365-246X.1973.tb02407.x, doi:10.1111/j.1365-246X.1973.tb02407.x.

Prøsch-Danielsen, L., 2006. Sea-level studies along the coast of southwestern Norway: with emphasise on three short-lived Holocene marine events. Number 20 in AmS-Skrifter, Arkeologisk Museum, Stavanger.

Quinlan, G., Beaumont, C., 1981. A comparison of observed and theoretical postglacial relative sea level in Atlantic Canada. Canadian Journal of Earth Sciences 18, 1146–1163. URL: http://www.nrcresearchpress.com/doi/10.1139/e81-109, doi:10.1139/e81-109.

Quinlan, G., Beaumont, C., 1982. The deglaciation of Atlantic Canada as reconstructed from the postglacial relative sea-level record. Canadian Journal of Earth Sciences 19, 2232–2246. URL: http://www.nrcresearchpress.com/doi/10.1139/e82-197, doi:10.1139/e82-197.

Rasmussen, H., Bondevik, S., Corner, G.D., 2018. Holocene relative sea level history and Storegga tsunami run-up in Lyngen, northern Norway. Journal of Quaternary Science 33, 393–408. URL: https://onlinelibrary.wiley.com/doi/10.1002/jqs.3021, doi:10.1002/jqs.3021.

Romundset, A., Bondevik, S., Bennike, O., 2011. Postglacial uplift and relative sea level changes in Finnmark, northern Norway. Quaternary Science Reviews 30, 2398–2421. URL: https://linkinghub.elsevier.com/retrieve/pii/S027737911100179X, doi:10.1016/j.quascirev.2011.06.007.

Romundset, A., Lakeman, T.R., Høgaas, F., 2018. Quantifying variable rates of postglacial relative sea level fall from a cluster of 24 isolation basins in southern Norway. Quaternary Science Reviews 197, 175–192. URL: https://www.sciencedirect.com/science/article/pii/S0277379118302890, doi:10.1016/j.quascirev.2018.07.041.

Romundset, A., Lohne, N.S., Mangerud, J., Svendsen, J.I., 2010. The first Holocene relative sea-level curve from the middle part of Hardangerfjorden, western Norway. Boreas 39, 87–104. URL: https://onlinelibrary.wiley.com/doi/abs/10.1111/j.1502-3885.2009.00108.x, doi:10.1111/j.1502-3885.2009.00108.x. _eprint: https://onlinelibrary.wiley.com/doi/pdf/10.1111/j.1502-3885.2009.00108.x.

Rosentau, A., Grudzinska, I., Kalińska, E., Alexanderson, H., Bērziņš, V., Ceriņa, A., Kalniņa, L., Karušs, J., Lamsters, K., Muru, M., Nartišs, M., Paparde, L., Hang, T., 2023. Holocene relative shore-level changes and development of the Ģipka lagoon in the western Gulf of Riga. Boreas 52, 517–537. URL: https://onlinelibrary.wiley.com/doi/10.1111/bor.12628, doi:10.1111/bor.12628.

Rosentau, A., Klemann, V., Bennike, O., Steffen, H., Wehr, J., Latinović, M., Bagge, M., Ojala, A., Berglund, M., Becher, G.P., Schoning, K., Hansson, A., Nielsen, L., Clemmensen, L.B., Hede, M.U., Kroon, A., Pejrup, M., Sander, L., Stattegger, K., Schwarzer, K., Lampe, R., Lampe, M., Uścinowicz, S., Bitinas, A., Grudzinska, I., Vassiljev, J., Nirgi, T., Kublitskiy,

Y., Subetto, D., 2021. A Holocene relative sea-level database for the Baltic Sea. Quaternary Science Reviews 266, 107071. URL: https://linkinghub.elsevier.com/retrieve/pii/S027737912100278X, doi:10.1016/j.quascirev.2021.107071.

Rosentau, A., Muru, M., Kriiska, A., Subetto, D.A., Vassiljev, J., Hang, T., Gerasimov, D., Nordqvist, K., Ludikova, A., Lõugas, L., Raig, H., Kihno, K., Aunap, R., Letyka, N., 2013. S tone A ge settlement and H olocene shore displacement in the N arva- L uga K lint B ay area, eastern G ulf of F inland. Boreas 42, 912–931. URL: https://onlinelibrary.wiley.com/doi/10.1111/bor.12004, doi:10.1111/bor.12004.

Roy, K., Peltier, W., 2015. Glacial isostatic adjustment, relative sea level history and mantle viscosity: reconciling relative sea level model predictions for the U.S. East coast with geological constraints. Geophysical Journal International 201, 1156–1181. URL: http://academic.oup.com/gji/article/201/2/1156/579933/Glacial-isostatic-adjustment-relative-sea-level, doi:10.1093/gji/ggv066.

Roy, K., Peltier, W., 2017. Space-geodetic and water level gauge constraints on continental uplift and tilting over North America: regional convergence of the ICE-6G_c (VM5a/VM6) models. Geophysical Journal International 210, 1115–1142. URL: https://academic.oup.com/gji/article-lookup/doi/10.1093/gji/ggx156, doi:10.1093/gji/ggx156.

Roy, K., Peltier, W.R., 2018. Relative sea level in the Western Mediterranean basin: A regional test of the ICE-7G_na (VM7) model and a constraint on late Holocene Antarctic deglaciation. Quaternary Science Reviews 183, 76–87. URL: https://www.sciencedirect.com/science/article/pii/S027737911730642X, doi:10.1016/j.quascirev.2017.12.021.

Rudolph, M.L., Lekić, V., Lithgow-Bertelloni, C., 2015. Viscosity jump in Earth's mid-mantle. Science 350, 1349–1352. URL: https://www.science.org/doi/full/10.1126/science.aad1929, doi:10.1126/science.aad1929. publisher: American Association for the Advancement of Science.

Shennan, I., Bradley, S.L., Edwards, R., 2018. Relative sea-level changes and crustal movements in Britain and Ireland since the Last Glacial Maximum. Quaternary Science Reviews 188, 143–159. URL: https://linkinghub.elsevier.com/retrieve/pii/S0277379118300040, doi:10.1016/j.quascirev.2018.03.031.

Shugar, D.H., Walker, I.J., Lian, O.B., Eamer, J.B., Neudorf, C., McLaren, D., Fedje, D., 2014. Post-glacial sea-level change along the Pacific coast of North America. Quaternary Science Reviews 97, 170–192. URL: https://linkinghub.elsevier.com/retrieve/pii/S0277379114002030, doi:10.1016/j.quascirev.2014.05.022.

Smith, D., Harrison, S., Firth, C., Jordan, J., 2011. The early Holocene sea level rise. Quaternary Science Reviews 30, 1846–1860. URL: https://linkinghub.elsevier.com/retrieve/pii/S0277379111001211, doi:10.1016/j.quascirev.2011.04.019.

Snyder, J.A., Korsun, S.A., Forman, S.L., 1996. Postglacial emergence and the Tapes transgression, north-central Kola Peninsula, Russia. Boreas 25, 47–56. URL: https://onlinelibrary.wiley.com/doi/10.1111/j.1502-3885.1996.tb00834.x, doi:10.1111/j.1502-3885.1996.tb00834.x.

Steffen, H., Kaufmann, G., 2005. Glacial isostatic adjustment of Scandinavia and northwestern Europe and the radial viscosity structure of the Earth's mantle. Geophysical Journal International 163, 801–812. URL: https://academic.oup.com/gji/article-lookup/doi/10.1111/j.1365-246X.2005.02740.x, doi:10.1111/j.1365-246X.2005.02740.x.

Strandberg, N.A., Barliaev, A., Martinsson-Wallin, H., Risberg, J., Hättestrand, M., Croudace, I., Kylander, M., Yokoyama, Y., 2020. Landscape development at Lina myr fen, Eastern Gotland, 9000-2500 cal. yr BP. The Holocene 30, 1205–1219. URL: http://journals.sagepub.com/doi/10.1177/0959683620913919, doi:10.1177/0959683620913919.

Svendsen, J.I., Mangerud, J., 1987. Late Weichselian and holocene sea-level history for a cross-section of western Norway. Journal of Quaternary Science 2, 113–132. URL: https://onlinelibrary.wiley.com/doi/10.1002/jqs.3390020205, doi:10.1002/jqs.3390020205.

Vacchi, M., Engelhart, S.E., Nikitina, D., Ashe, E.L., Peltier, W.R., Roy, K., Kopp, R.E., Horton, B.P., 2018. Postglacial relative sea-level histories along the eastern Canadian coastline. Quaternary Science Reviews 201, 124–146. URL: https://linkinghub.elsevier.com/retrieve/pii/S0277379118300209, doi:10.1016/j.quascirev.2018.09.043.

Waelbroeck, C., Labeyrie, L., Michel, E., Duplessy, J.C., McManus, J.F., Lambeck, K., Balbon, E., Labracherie, M., 2002. Sea-level and deep water temperature changes derived from benthic foraminifera isotopic records. Quaternary Science Reviews 21, 295–305. URL: https://www.sciencedirect.com/science/article/pii/S0277379101001019, doi:10.1016/S0277-3791(01)00101-9.

Wessel, P., Luis, J.F., Uieda, L., Scharroo, R., Wobbe, F., Smith, W.H.F., Tian, D., 2019. The Generic Mapping Tools Version 6. Geochemistry, Geophysics, Geosystems 20, 5556–5564. URL: https://agupubs.onlinelibrary.wiley.com/doi/10.1029/2019GC008515, doi:10.1029/2019GC008515.

Yu, S.Y., Berglund, B.E., Sandgren, P., Lambeck, K., 2007. Evidence for a rapid sea-level rise 7600 yr ago. Geology 35, 891. URL: https://pubs.geoscienceworld.org/geology/article/35/10/891-894/129673, doi:10.1130/G23859A.1.

Zwartz, D., Bird, M., Stone, J., Lambeck, K., 1998. Holocene sea-level change and ice-sheet history in the Vestfold Hills, East Antarctica. Earth and Planetary Science Letters 155, 131–145. URL: https://www.sciencedirect.com/science/article/pii/S0012821X97002045, doi:10.1016/S0012-821X(97)00204-5.

Supplementary Figures

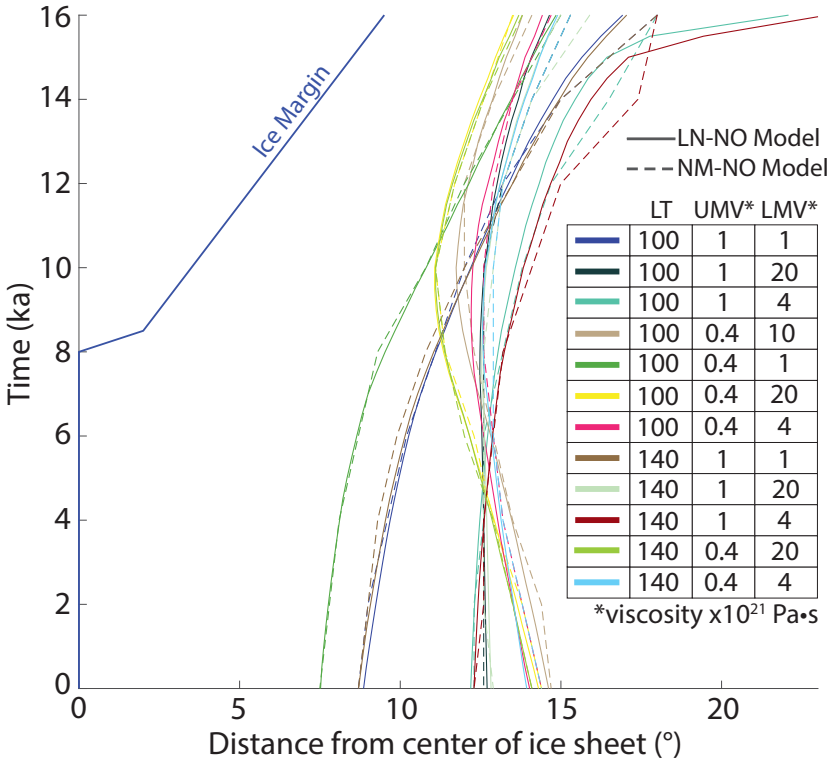

Figure S1: **LN-NO and NM-NO model predictions for the evolution of the solid Earth hinge line during the deglaciation of a synthetic disc load.** The NM-NO and LN-NO models are run at spherical harmonic degrees 128 and 256, respectively. The models include no ocean. Parameters for each simulation are indicated in the inset. The position of the ice margin is shown by a dark blue line.

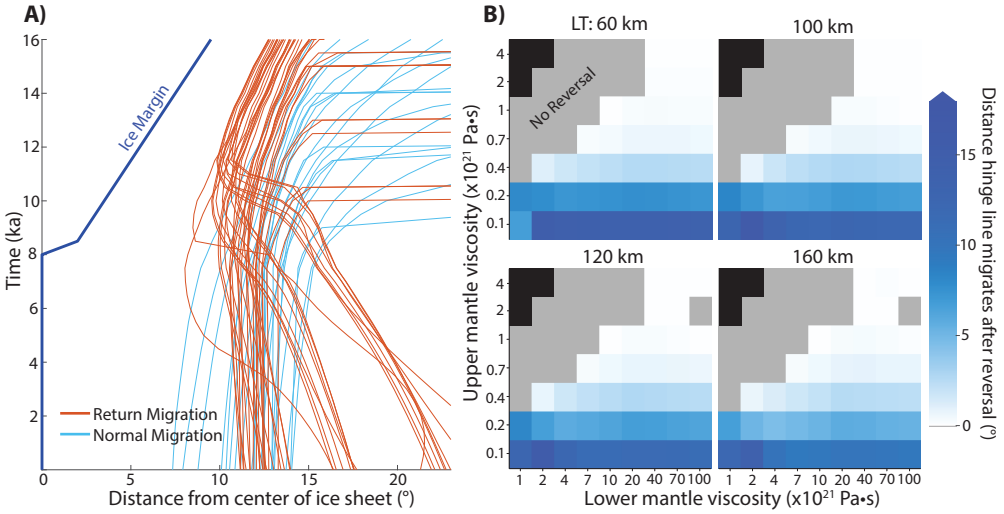

Figure S2: **Results from the LN-NO model as in Figure 4 of the main text, but including the modeled change in the geoid in predictions of the 'hinge line'.** In this case, the 'hinge line' can be thought of as the line delineating the rise and fall of a hypothetical ocean although no ocean is included in the model. Including gravity changes does not substantially change the behavior of the hinge line shown in Figure 4.

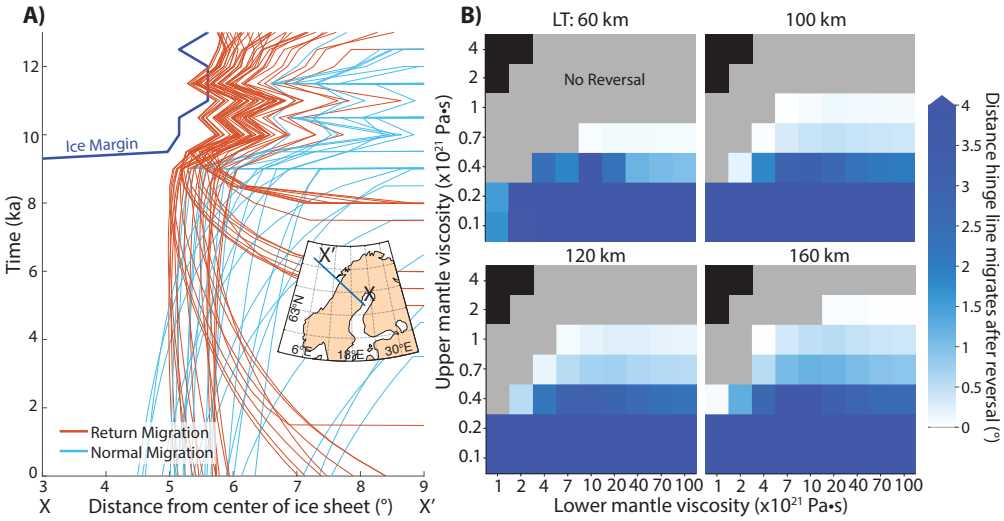

Figure S3: **Results from the LN-NO model as in Figure 5 of the main text, but including the modeled change in the geoid in predictions of the 'hinge line'.** In this case, the 'hinge line' can be thought of as the line delineating the rise and fall of a hypothetical ocean although no ocean is included in the model. Note, including gravity changes does not substantially change the behavior of the hinge line shown in Figure 5.

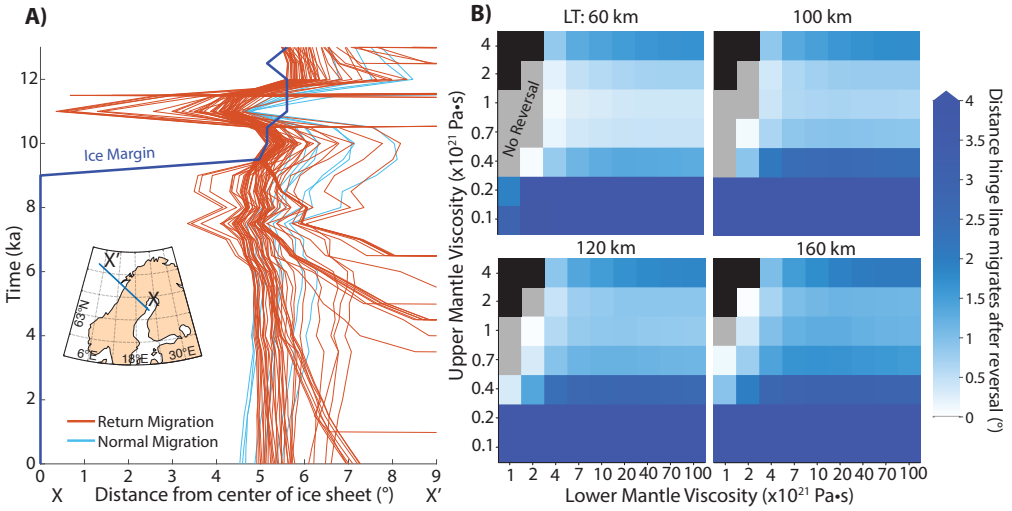

Figure S4: **Results from the LN-NO code as in Figure 5 of the main text, but including all the ice sheets in the ICE7G reconstruction.** Distant ice sheets (mainly the LIS) create a large excursion in hinge line evolution during the Younger Dryas (12-11.5 ka, A). In simulations with high upper mantle viscosities ($2 - 4 * 10^{21}$ Pa s), distant ice sheets also have a subtle influence on hinge line migration during the middle to late Holocene (A) and can result in reverse migration (B). Note, both plots show only the solid Earth component of deformation; gravity changes due to mass changes are not included.

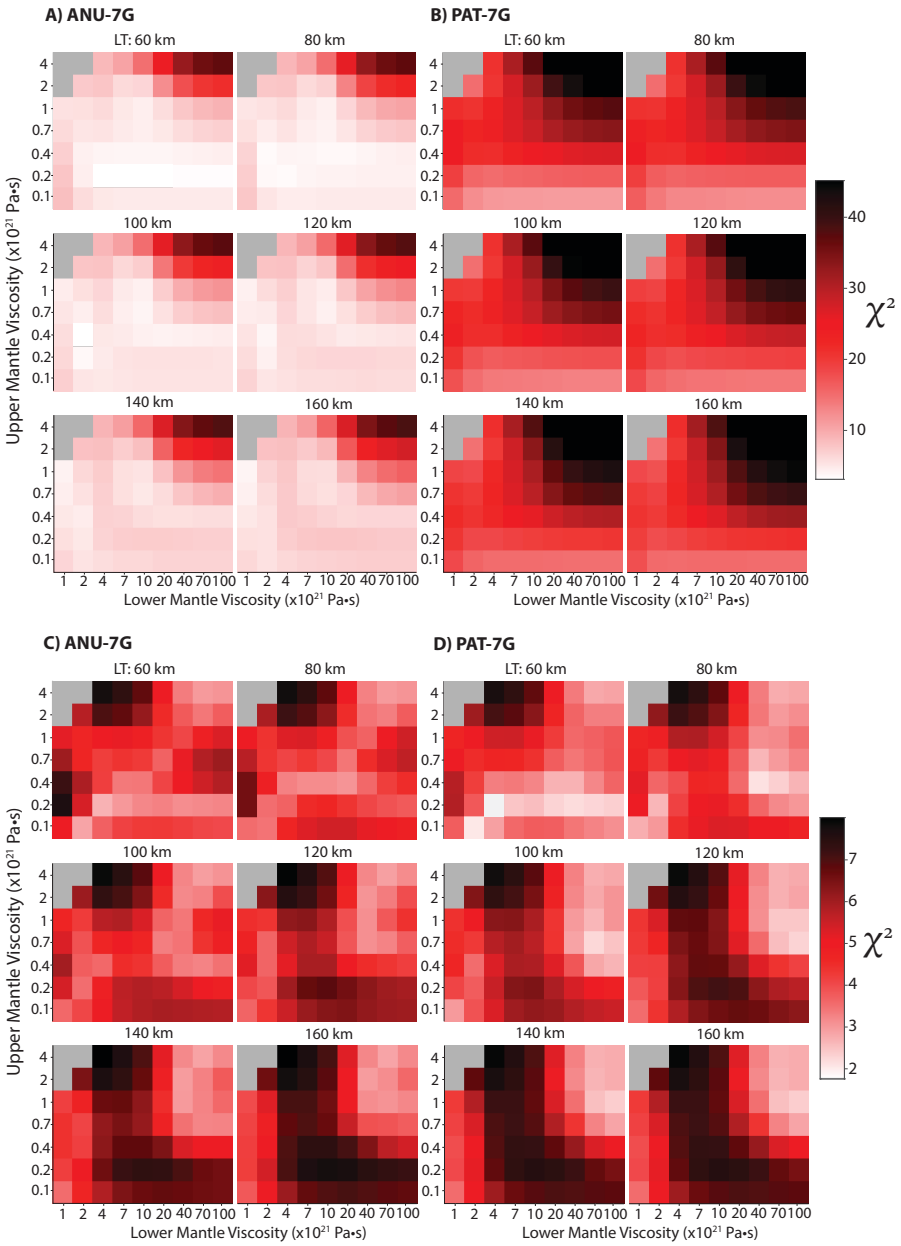

Figure S5: **As in Figure 7, chi-squared distributions for the comparison between LN-SL models and the sea-level data sets.** Results are shown for Norway (A,B) and Eastern Canada (C,D), but for the ice models ANU-7G (A,C) and PAT-7G (B,C).

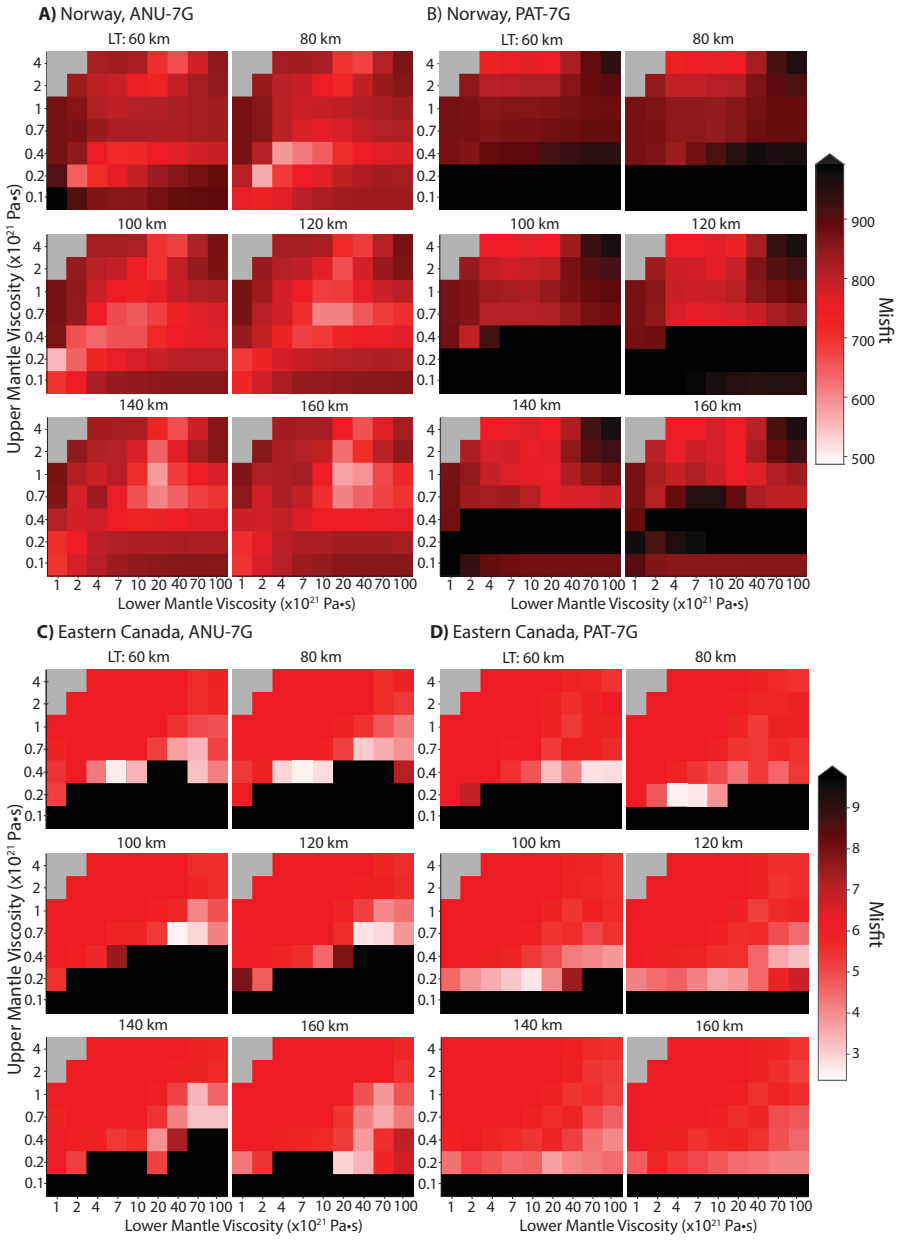

Figure S6: **As in Figure 8, GIA model (LN-SL) misfit for the goodness-of-fit test to the STEHMs of transgression magnitude.** Results are shown for Norway (A,B) and Eastern Canada (C,D), but for the ice models ANU-7G (A,C) and PAT-7G (B,C).